QUANTITATIVE DEDICATED CONE BEAM BREAST CT IMAGING

A Dissertation
Presented to
The Academic Faculty

by

Linxi Shi

In Partial Fulfillment
of the Requirements for the Degree
Doctor of Philosophy
in
The George W. Woodruff School of Mechanical Engineering
Nuclear & Radiological Engineering & Medical Physics

Georgia Institute of Technology
[AUGUST 2017]

QUANTITATIVE DEDICATED CONE BEAM BREAST CT IMAGING

Approved by:

Dr. Lei Zhu, Advisor
School of Mechanical Engineering
Nuclear & Radiological Engineering & Medical Physics
Georgia Institute of Technology

Dr. Xiangyang Tang
Department of Biomedical Engineering
Georgia Institute of Technology
&
Department of Radiology and Imaging Sciences
Emory University

Dr. C.-K. Chris Wang
School of Mechanical Engineering
Nuclear & Radiological Engineering & Medical Physics
Georgia Institute of Technology

Dr. John N. Aarsvold
Department of Radiology and Imaging Sciences
Emory University
&
Nuclear Medicine Service
Atlanta Veterans Affairs Medical Center

Dr. Justin Roper
School of Mechanical Engineering
Nuclear & Radiological Engineering & Medical Physics
Georgia Institute of Technology
&
Department of Radiation Oncology
Emory University

Date Approved: [April 07, 2017]

ACKNOWLEDGEMENTS

I thank all the people who have made my time at the Georgia Institute of Technology such a great experience. Without their guidance and support, I would not be here.

Especially I want to express gratitude to my advisor, Dr. Lei Zhu, without whose encouragement and support I would not have ventured over to pursue my Doctorate degree in the NRE/MP program. Knowing my interest in medical imaging and related prior experiences, Dr. Zhu encouraged me to aim high and expressed willingness to take me as his Ph.D. student. He is a dedicated mentor, always willing to take time out of his schedule and discuss the projects with me. His instruction on many topics has led to fruitful conversation and many new research directions. His excitement about research has been a very positive influence on my current work and future career goal. Working with Dr. Zhu had a tremendous impact on my education and I cannot thank him enough for his patience, knowledge, understanding and guidance.

I thank Dr. Andrew Karellas and Dr. Srinivasan Vedantham for their collaboration of this project. They were absolutely essential for this Ph.D. work. Without them providing the invaluable clinical data on breast CT, this work would not have been possible.

I appreciate the help of my lab mate Tonghe Wang, who has helped me to become familiar with all the software and hardware developed before my arrival. Tonghe also worked closely with me on the phantom study presented in this work progress of this project was greatly expedited with his assistance.

I also want to thank the rest of my committee members, Dr. Chris Wang, Dr. Justin Roper, Dr. Xiangyang Tang and Dr. Dr. John N. Aarsvold, for their support and assistance on this work. Without their invaluable feedback and advice, this work would not have been gone so smooth.

Finally, with love, I thank my parents and all my amazing friends for providing encouragement, support, and invaluable flexibility and fun during the most challenging times.

TABLE OF CONTENTS

LIST OF TABLES

LIST OF FIGURES

LIST OF SYMBOLS AND ABBREVIATIONS

Dedicated Cone Beam Breast Computed Tomography	CBBCT
Library-Based	LB
Forward-Projection-Based	FP
Off-Focus Radiation	OFR
Magnetic Resonance Imaging	MRI
Digital Breast Tomosynthesis	DBT
Molecular Breast Imaging	MBI
Cone Beam Computed Tomography	CBCT
Monte Carlo	MC
Spatial Non-Uniformity	SNU
Contrast to Signal Deviation Ratio	CDR
Contrast to Noise Ratio	CNR
Volumetric Glandular Fraction	VGF
Source to Axis of Rotation Distance	SAD
Source to Detector Distance	SDD
Center of Mass	COM
Region of Interest	ROI
Breast Imaging-Reporting and Data System	BI-RADS
American College of Radiology	ACR
Thallium-Doped Cesium Iodine	CsI:Tl
Kernel-based Fuzzy C-mean	KFCM
Root Mean-Square Difference	RMSD

Planning Computed Tomography	pCT
X-ray Flat Field Intensity	I_0
Point Spread Function	PSF
Line Spread Function	LSF
Edge Spread Function	ESF
Modulation Transfer Function	MTF

SUMMARY

In the United States, annual mammogram screening for early breast cancer detection is recommended. Such screening is known to have a significant impact on improving cancer mortality rates. However, the diagnostic function of mammogram is hampered due to their being two-dimensional projections, resulting in tissue superposition and compromised specificity and sensitivity. Dedicated cone beam breast computed tomography (CBBCT) is a recently approved diagnostic tool that produces high quality tissue-superposition-free volumetric images, demonstrating a potential to substantially improve breast cancer detection and diagnosis. Nevertheless, high scatter contamination stemming from large irradiation volume results in severe contrast lost and shading artifacts, impeding the quantitative uses of CBBCT in certain clinical tasks. Existing scatter correction methods demonstrate different drawbacks including low efficacy, dose or scan time increase, etc. In this thesis, we propose two scatter correction methods, library-based (LB) and forward-projection-based (FPB), to overcome the deficiencies while achieving high correction efficacy.

In the LB method, a scatter library is precomputed via Monte Carlo simulation based on a simple breast model. Due to the relatively simple shape and composition, we find that a small library size with one input parameter of breast size is sufficient for effective scatter correction on general population. In the FPB method, we first estimate primary signals of CBBCT projections via forward projection of the segmented first-pass reconstruction. By subtracting the simulated primary projection from the raw projection, we obtain a raw scatter estimate containing both low-frequency scatter and errors. After

discarding untrusted errors from the resultant raw scatter map, the final scatter is obtained via a novel Fourier-transform based local filtration algorithm. Both methods have demonstrated high correction efficacy on patient data, the LB method is superior in computational efficiency while the FPB method has better flexibility.

By comparing these two proposed methods, we find that there is a large discrepancy between the scatter estimation of the two; and the FPB method tends to better preserve high spatial-resolution details than the LB method. We hypothesize that this is mainly due to the existence of off-focus radiation (OFR), which is a fundamental factor degrading the image spatial resolution. To quantitatively investigate the effect of OFR on spatial resolution, we designed an experiment to characterize the spatial resolution with and without OFR. The obtained results are consistent with the correction results using the two correction methods, therefore successfully validating our hypothesis.

CHAPTER 1. INTRODUCTION

1.1 Current State of Diagnostic Breast Imaging

Breast cancer is the most common cancer in women worldwide and the second leading cause of cancer induced death in women today[1, 2]. From an imaging perspective, mammography has been considered as "gold standard" in detecting breast cancer at a more treatable stage[3, 4]. However, mammography has limited sensitivity and specificity due to the imposed tissue superposition, especially for women with dense breast [5, 6]. Many other imaging technologies are developed as an adjunct to improve diagnosis in breast cancer detection, including ultrasound, magnetic resonance imaging (MRI), digital breast tomosysthesis (DBT) as well as molecular breast imaging (MBI)[7-9]. In this section, the role of each imaging modality in diagnosis of breast cancer will be briefly introduced.

Breast ultrasound is routinely used for differentiating cysts from solid tumors, and many benign solid abnormalities from malignancies with high specificity [10-14]. The widespread availabilities and inexpensive medical bills make it a major adjunctive mode of imaging for breast cancer diagnosis. One disadvantage is that the effectiveness of breast ultrasound is highly dependent on operator's skills. Another disadvantage is that it has lower specificity in differentiating between certain solid masses and has limited ability to visualize deep tumors[14, 15].

Breast MRI is not a replacement for mammography and ultrasound but a supplement tool for detecting breast cancers that are hard to distinguish from the previous two modalities[16, 17]. Breast MRI is non-ionizing, possesses excellent sensitivity and

independent of breast density. However, it is expensive and for most of the time requires injection of contrast agent for functional imaging. It cannot be used for patients with pacemakers or metal implants. The specificity of breast MRI can also be limited, it is highly sensitive to small abnormalities but cannot visualize calcifications due to its lack of hydrogen. It takes a longer time to obtain MRI images than other imaging modalities and therefore can induce claustrophobia[18-20].

DBT is x-ray tomographic system with limited projection angle that can partially eliminate the tissue superposition in mammography[21-25]. The DBT system has been recently approved by the FDA for clinical use to perform breast cancer screening exams. It demonstrates widespread adaptability in clinical setting due to its similarity to mammogram in terms of image type and patient positioning. Initial clinical studies of DBT exhibit potentials to decrease the false positive recall rate and slightly improve the sensitivity and accuracy in invasive cancer detection with higher improvements seen in women with denser breasts. However, the DBT's ability in visualizing calcifications is hampered by its limited projection angle. As a result, the standard mammography images must be also obtained during imaging acquisition, potentially increasing the scanning time and dose [21, 25-27].

MBI applies nuclear medicine technique that uses γ-camera in mammographic mode to provide functional images of the breast. Early studies show that the sensitivity of MBI is higher than MRI without an issue of pacemaker and metal implants encountered in MRI imaging[28]. MBI also performs excellence in detecting metastatic cancer[29, 30]. However, the use of MBI requires the injection of radioactive substances, which lead to

increased radiation comparing to a mammography. Another disadvantage is its sensitivity is low in detecting small abnormalities below 1 cm[31].

Recognizing the limitations in mammography, all the above-mentioned imaging modalities serve to assist in enhancing the diagnostic accuracy of breast cancer. However, each modality is only most beneficial when utilized by considering individual characteristics such as age, risk, and breast density.

1.2 The Role of Dedicated CBBCT in Cancer Diagnosis

1.2.1 Overview of Cone Beam Computed Tomography (CBCT)

Cone beam CT is a recently developed technology. Unlike conventional multi-slice CT using either fan beam or spiral-scan geometries, CBCT uses a cone shaped x-ray beam and a flat panel detector. The x-ray source and detector are fixed to each other on a gantry which rotates around a fixed axis of rotation for data acquisition. During the CBCT scanning, multiple planar projection images of the whole irradiated volume are obtained in either a complete or partial rotation. The entire volumetric images can be reconstructed via FDK algorithm in one rotation. This procedure varies from a multi-slice CT, where a fan-shaped beam in a helical mode is used to acquire and reconstruct each slice of the imaged volume and then stack them together for a 3D representation[32] (Fig 1).

The CBCT is initially developed for angiography [33]. The advantages for such a system include larger volume coverage, therefore no need of translation of the patient during scanning, and high spatial resolution due to the use of flat panel detector[34]. As the technologies marched on, CBCT has been increasingly demanded in various clinical

applications, including radiotherapy guidance[35, 36], dental imaging[32, 34] as well as intervention radiology. And in recent years, researchers have been applying the cone beam technology to design the CT system dedicated solely for breast imaging.

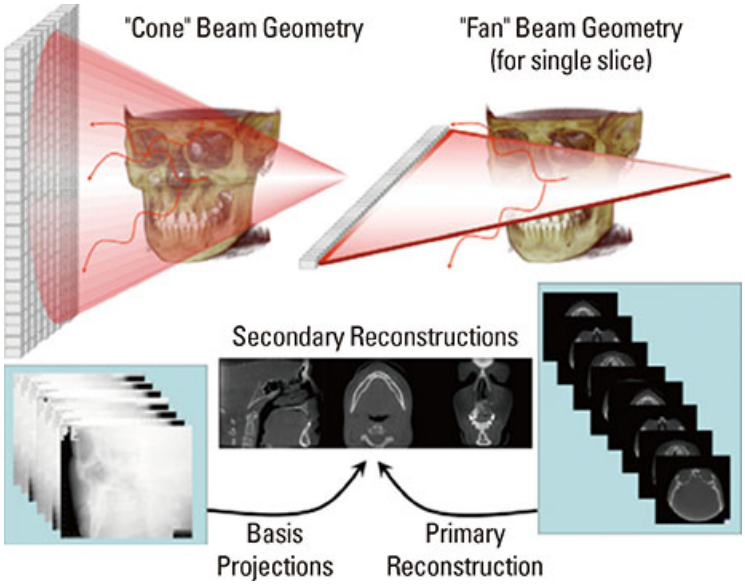

Fig 1 Data acquisition comparison between the conventional or ‘‘fan’’ beam (right) and ‘‘cone’’ beam (left) imaging geometry and resultant image production. (Courtesy: Scarfe WC, Farman AG. “What is cone beam CT and how does it work?”. Dent Clin North Am, 52(4),707-30, 2008)

1.2.2 Overview of Dedicated cone beam breast CT (CBBCT)

Breast cancer can be masked in projection-based mammography due to tissue superposition, especially in women with dense breasts[37]. CBBCT system with flat panel detector can resolve the tissue superposition at a comparable dose of diagnostic mammography[38] [39]. Fig 2 shows a case with dense breast, where the lesion is masked in mammogram but clearly revealed in CBBCT image.

Recently, CBBCT (manufactured by Koning Corporation, West Henrietta, NY, USA) was approved by FDA to perform diagnostic breast imaging. The schematic drawing

of this system is shown in Fig 3. During the imaging acquisition, the patient lies prone on a bench table with an aperture, through which the breast hangs in the pendant position without physical compression as used mammogram. Underneath the table, an X-ray tube and a flat-panel detector rotate around the breast, acquiring cone-beam projection images (Fig 4) [38].

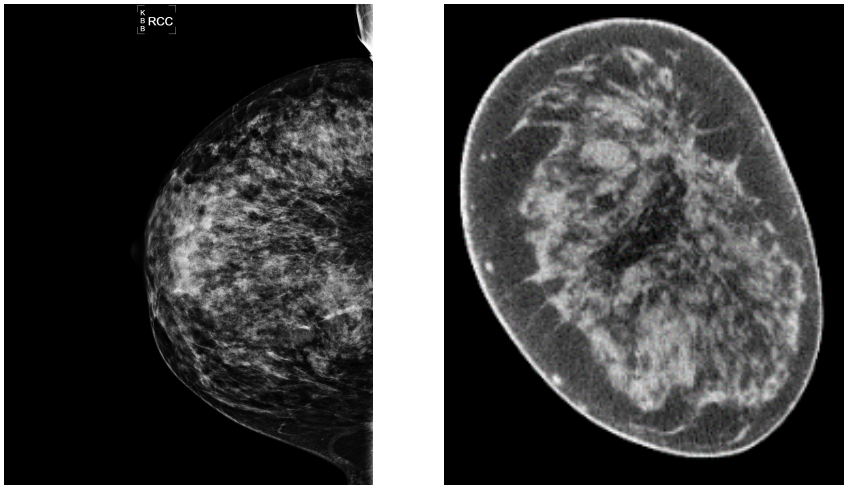

Fig 2 Left. The mammogram of a patient with dense breast. Right. Corresponding CBBCT image shows a large lesion that is disguised in mammogram.

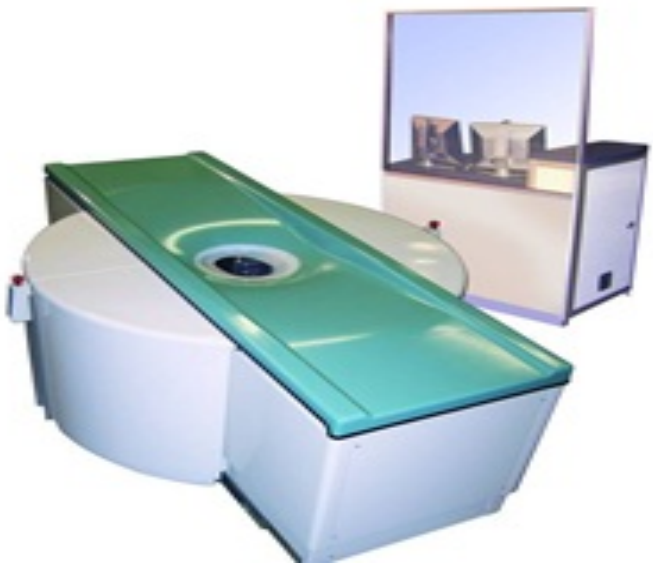

Fig 3 The dedicated CBBCT system manufactured by Koning Corporation.

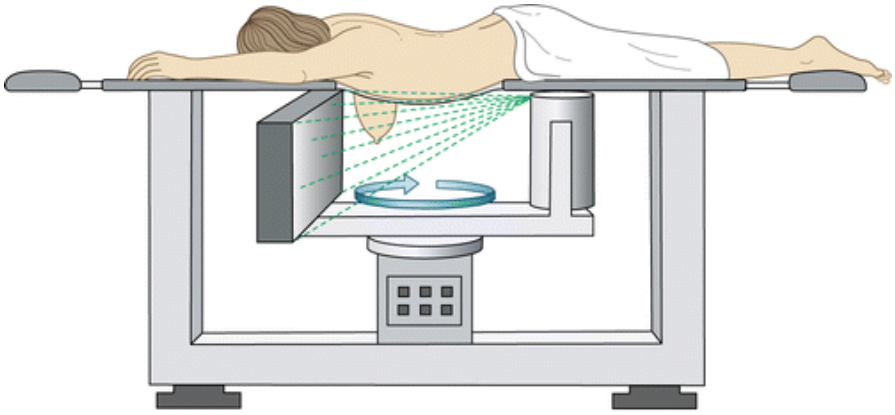

Glick SJ. 2007.
Annu. Rev. Biomed. Eng. 9:501–26

Fig 4 Schematic drawing of the CBBCT system. (Courtesy: Stephen J. Glick. "Breast CT". Annu. Rev. Biomed. Eng. 9:501–26. 2007)

1.3 Challenges for Quantitative CBBCT Imaging

Although the CBBCT potentially improves the clinical performances in breast cancer diagnosis, a fundamental limitation of CBBCT image quality is the high scatter contamination stemming from the large irradiation volume in each x-ray projection.

The scatter-induced artifacts on CBBCT images manifest themselves as reduced signal intensities especially around the object center as well as degraded image contrast[40]. Fig 5 shows some typical scatter contaminated CBBCT images.

These CBBCT imaging errors cause inaccurate quantitative assessment in clinical tasks[41] and reduce sensitivity in calcification and lesion detection[42]. Scatter correction methods for cone beam CT (CBCT) in general have been extensively investigated over the past decades, and this research topic continues to be active due to the increasing demands of CBCT in different clinical applications.

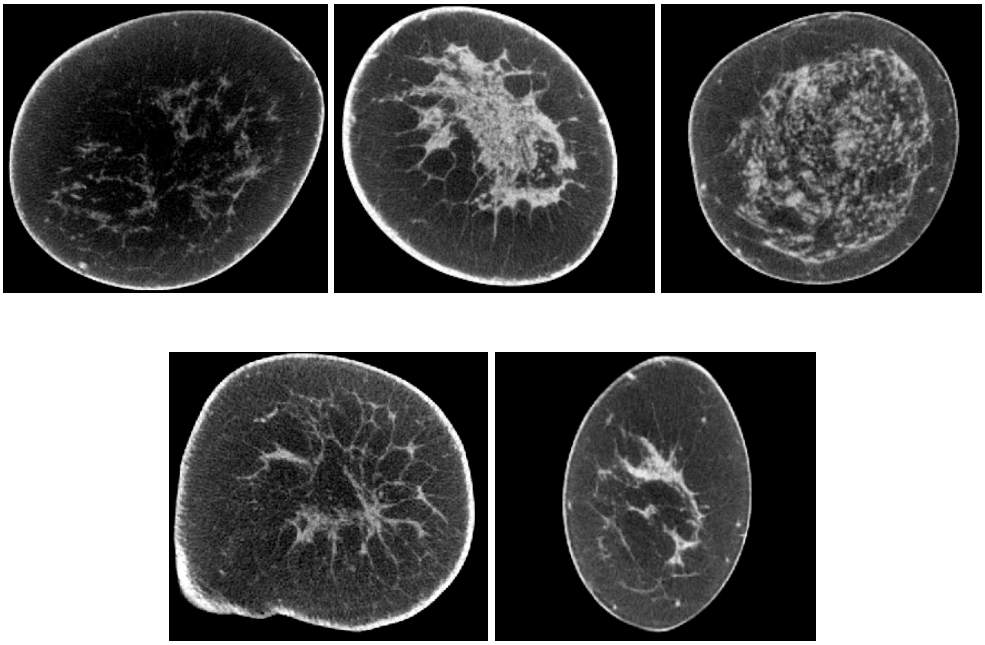

Fig 5 Scatter contaminated CBBCT images

1.4 Review of Existing Solutions

Suppression of scatter signals has been an active research field since the early days of x-ray and CT imaging[42-46]. Briefly, existing methods can be divided into two main categories: scatter rejection by preventing the scattered photons from reaching the detector [47-51] and scatter correction by estimating the scatter content after projection data acquisition. It is worth mentioning that the latter is only able to remove the mean scatter signals, leaving statistical scatter noise in the corrected images. Thus, it is inherently more dose-efficient to prevent scatter from reaching the detector than to correct for scatter on scatter contaminated projections. However, current scatter rejection methods using wither anti-scatter grid or air gap inevitably increase the dose to patients[51, 52]. The scatter correction methods can be further classified into three main categories: scatter rejection using analytical modelling[53-57], Monte Carlo (MC) simulation [58-63], and scatter measurement [43, 45, 64-67]. Comprehensive reviews of general scatter correction methods can be found in Refs.[49, 68, 69]. Despite their success demonstrated in certain scenarios, these methods have different drawbacks including low efficacy, dose or scan time increase, need for hardware modification, and intensive computation. An optimal scatter correction approach is yet to be established. In current CBBCT imaging, the most investigated method for scatter correction is probably scatter measurement. The measurement-based methods insert a sheet of beam-stop or beam-pass array to sparsely measure scatter or primary signals [42, 45, 70]. Scatter estimation is then obtained via interpolation, based on the fact that scatter contains dominant low-frequency components. In addition to modifications of the imaging geometry, due to the inevitable loss of primary

signals inside the blocker shadows, these methods require extra data acquisition and therefore additional imaging dose. Shading correction on CBBCT images as a post-reconstruction processing step removes global cupping artifacts[41, 71], but fails to reduce high-frequency image errors. The corrected images therefore still suffer from contrast loss.

1.5 Overview of this Thesis

In a clinical setting, the following properties are desired on a practical scatter correction method for CBBCT: 1) high correction efficacy and reliability across general populations; 2) no requirement of imaging time increase or imaging hardware modifications; 3) high computational efficiency. None of the existing approaches on CBBCT achieves the above three goals simultaneously.

This thesis proposes two scatter correction methods that can be easily adopted to clinical settings as a software plug. CHAPTER 2 describes a library-based (LB) scatter correction method, where a small scatter database is precomputed and can be used for scatter correction for entire women population. Forward projection based (FPB) scatter correction method with better flexibility is proposed in CHAPTER 3. In CHAPTER 4, the differences between the two methods are identified, composed and discussed. An interesting observation is made, which opens another research arena to be explored in the future. And CHAPTER 5 concludes the work that have completed in this thesis and specifically discusses the future investigation.

CHAPTER 2. LIBRARY-BASED SCATTER CORRECTION

2.1 Introduction

In this chapter, we aim to develop a practical technique for CBBCT by exploiting its unique feature of relatively small variations in scatter properties with heterogeneous tissue distribution and the relatively simple geometry of the imaged object (i.e. breast). Inspired by Ref.[43], where scatter database for one patient is pre-measured and modified for scatter correction of subsequent scans for the same patient, we propose to pre-compute a library of scatter distributions via Monte Carlo (MC) simulations on breasts with different dimensions. On patient data acquired from a clinical research prototype CBBCT system with no hardware modification or scan time increase, we first select the scatter distribution according to the breast size measured on a first-pass CBBCT reconstruction. The selected scatter distribution is modified to account for the geometric transformation between the MC simulation and the physical scan, and then subtracted from the measured projections for effective scatter correction. In general CT imaging, a large scatter library is needed for the success of the proposed method, especially for complex objects, increasing the computational burden. In CBBCT, however, we find that a scatter library with only one input parameter of the breast size, is sufficient for effective scatter correction. The computationally intensive MC simulation can therefore be greatly reduced. Furthermore, the MC simulations for generating the scatter library are pre-computed and do not need to be repeated for each patient dataset. The signal processing time for scatter correction is therefore much less than the CBBCT reconstruction time. We investigate the efficacy and

robustness of the proposed library-based scatter correction on 15 clinical research patient datasets, with a wide range of breast sizes and geometric complexities. Image spatial non-uniformity (SNU) and the separation in linear attenuation coefficients between adipose and fibroglandular tissue, herein referred to as contrast to signal deviation ratio (CDR) are used as quality metrics for evaluating the performance of the method.

2.2 Methods and Materials

2.2.1 Breast model and parameterization of the scatter library of CBBCT

Besides correction accuracy, the practical value of the proposed library-based method is determined by the size of the pre-computed library. On a CT scanner with a fixed imaging protocol, the scatter distribution is dependent on the unknown anatomical structures (i.e., shapes and heterogeneous distributions) of the imaged object. A large set of parameters are therefore needed to specify the object geometry, which in general can be arbitrary and complex, and hence, a large number of possible scatter distributions. In addition, each scatter distribution on a 2D detector of a CT scan has three dimensions: the lateral and longitudinal detector coordinates (u, v) as well as the projection angle β, which typically covers 360 degrees. As such, an ideal scatter library has a tremendously large size and requires huge memory consumption on a computer.

Although library-based scatter correction seems infeasible for general CT imaging, we find that the library size for effective scatter correction can be very small for breast imaging on the current clinical research CBBCT systems. Fig 6 shows the geometry of the clinical research CBBCT used in our studies[72]. The breast with a semi-ellipsoidal shape

is positioned pendant along the y-axis of rotation through an aperture in the patient support table, while the x-ray tube and detector rotate around the breast simultaneously to acquire the projection data. The reconstructed CT image of the breast typically resembles a simple semi-ellipsoid, with no other background objects. In addition to the relatively simple shape, another unique feature of the breast is that it is mainly composed of soft tissue, including glandular and adipose tissue. It has been shown that these two materials lead to small differences in the resulting scatter distributions [39]. We can therefore generate the library of scatter distributions for a simplified breast model with a semi-ellipsoidal shape and a homogenous composition. Note that, such a simplified model has also been implemented in previous studies to obtain the dosimetric characteristics of CBBCT [73-77].

In this work, we further simplify the breast model by assuming rotational symmetry about the rotation axis of the CBBCT. As shown in Fig 6, we assume that the breast is centered at the rotation axis and the lengths of principle axes are equal in the x and z directions, denoted as D_{eff}. Hereafter in this work, we refer to D_{eff} as the effective breast diameter. On a real breast CBBCT image, D_{eff} can be determined as the effective diameter of the breast at the chest-wall. The length of semi-principal axis in the y direction of the breast model, which is the distance from the chest wall to nipple, is set to $0.75 \cdot D_{eff}$. The breast composition is modeled as a homogenous fibroglandular/adipose mixture with different densities simulating the effects of different volumetric glandular fractions (VGF). As shown in a later section, our investigations reveal that the performance of the proposed library-based scatter correction is insensitive to the breast density value used in our model. Therefore, we fix VGF as 15% (i.e., the population average [78, 79]) in the generation of the scatter library, unless otherwise stated. Note that, due to the rotational symmetry of the

breast model, the resultant scatter remains unchanged for different projection angles. As such, only one 2D image is needed to describe the scatter distribution for a CBBCT scan for one specific breast size. The pre-computed scatter library consists of a set of 2D scatter images for different D_{eff}, each denoted as $S_{D_{eff}}(u, v)$.

After aggressive simplification of the breast geometry, the scatter library has a small size with only one input parameter, D_{eff}. We will validate the proposed empirical breast model for scatter generation on patient data. One particular concern regarding the inaccuracy of our approach is the chest wall, which is not included in the breast model. As shown later in the evaluation studies, we find that ignoring the chest wall in the breast model has negligible effect on the scatter correction performance, mainly due to the strong signal attenuation in the chest wall region.

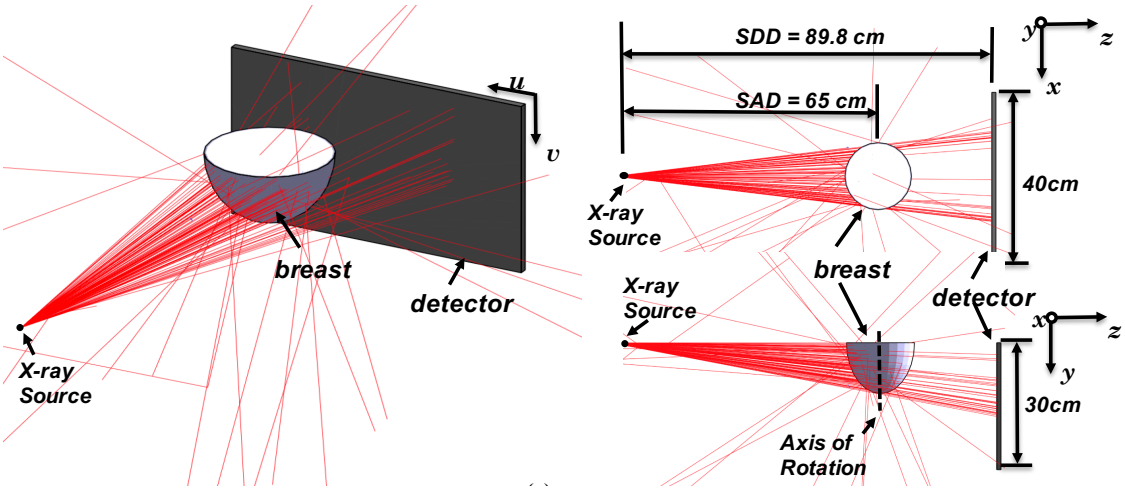

Fig 6 Imaging geometry of the clinical research CBBCT system used in the presented studies.

2.2.2 Library based scatter correction for CBBCT

2.2.2.1 Scatter Library Generation

Different methods, such as scatter measurement [64, 66, 70] or analytical modeling [80, 81], can be used to obtain scatter distributions on the simplified breast model. In this work, we choose to use the C++ based Geant4 Monte Carlo toolkit (www.geant4.org) to generate our scatter library.

Fig 6 shows screen shots of the MC simulation. In the simulation, we use the geometry of the clinical research prototype CBBCT system on which the patient data are acquired. The source to axis of rotation distance (SAD) is 65 cm and the source to detector distance (SDD) is 89.8 cm, resulting in a magnification factor of 1.38. The detector model is based on an ideal flat-panel detector with a dimension of 30 cm by 40 cm. To reduce the variance in the scatter estimate, we use a large pixel size of 1mm. The simulated photons are emitted from a point x-ray source to irradiate the entire breast with a half cone beam shape. Note that we do not model the bowtie filter as the system used to acquire the clinical datasets does not employ one.

To acquire $S_{D_{eff}}(u, v)$, a series of monoenergetic simulations are performed with photon energy ranging from 10 keV to the kVp value used in the clinical research CBBCT system, in increments of 2 keV. The Livermore low energy physics model of Geant4 is used for radiation transport. The physical processes for x-ray photon interactions include photo-electric effect, Compton scattering, and Rayleigh scattering. For each simulation, a total number of 1.2×10^7 photons per energy bin are emitted from the point source and the physical interactions are tracked along their trajectories. Position-dependent scatter and primary x-ray photon fluence incident on the detector are recorded. The scoring methodology is based on the interaction type, where each x-ray photon reaching the

detector is considered as a scatter event if it undergoes at least one scatter (Compton or Rayleigh scatter) interaction. For a primary event, the incident x-ray photon must satisfy the following conditions:1) it does not undergo Compton or Rayleigh scatter, (2) its energy does not change before hitting on the detector and (3) its direction does not change. The scatter distribution for a polyenergetic x-ray beam is generated by weighting the map from each energy bin with the x-ray spectrum normalized to unit area that is used for data acquisition.

MC simulation is computationally intensive, with the total simulation time proportional to the number of emitted photons. The simulated scatter distribution contains Poisson noise. An open-source Matlab function, Gridfit [82], is applied to reduce the noise on the scatter map via surface fitting in a similar way as in the existing literature [60, 61]. The Gridfit function is based on the concept of "approximant" map and it controls the amount of smoothness via a smoothing parameter, which is empirically chosen to minimize the root mean square difference in the scatter distribution prior to and after fitting. The resultant scatter distribution is considered noise-free and is finally archived in the scatter library.

The aforementioned methods are repeated for different D_{eff} to generate the entire scatter library. As shown in the evaluation studies, we find that the performance of the proposed scatter correction does not require a high accuracy of the D_{eff} value. Considering the range of D_{eff} in the general population, we use 6 cm to 22 cm, with an interval of 2 cm. The scatter library therefore consists of nine scatter images, each with a size of 1024 by 768 pixels after interpolating the original map with a size of 400 by 300. The total

computation time of the library generation is about 30 hours on a 2.5 GHz Intel Core i7 MacBook. Note that, this computation cost should be considered as part of the system calibration or pre-computation stage. Once the library is generated, it can be repetitively used for scatter correction on different patient datasets.

2.2.2.2 Library-based Scatter Estimation on Patient Data

We propose two steps to obtain an estimated scatter distribution for each patient dataset based on the pre-computed scatter library. First, we select a proper scatter distribution from the scatter library with a D_{eff} value matching that of the imaged breast. Second, the selected scatter distribution is modified to compensate for the difference in breast geometry between that used in MC simulation and that of the real breast.

2.2.2.2.1 Library selection scheme

Only one parameter, D_{eff}, is needed to select a scatter distribution from the scatter library. To select the appropriate D_{eff}, we perform a first-pass CBBCT reconstruction on the scatter-contaminated projections. The chest wall region is then segmented from the reconstructed volume. For the coronal slice closest to the chest-wall, the number of voxels within the breast, A, is determined and with known voxel dimension of ΔV, we estimate D_{eff} as in Ref. [83]:

$$D_{eff} = 2\times\Delta V \times\sqrt{A/\pi} \quad (1)$$

2.2.2.2.2 Scatter Modification Based on Object Translation and Magnitude Conversion

During MC simulation, the semi-ellipsoidal breast is centered at the rotation of axis. This condition, however, may not necessarily hold in a patient scan. Although the breast aperture on the clinical research CBBCT system is centered at the rotation of axis, variation in patient positioning results in translation of breast from the rotation axis. To compensate for the effects of different breast center positions in the simulated MC data and in the patient scan, we assume that the scatter distribution translates with the projection of the object center on the detector with an unchanged shape. Although this shift-invariance property is theoretically inaccurate for a divergent x-ray projection, our previous publication has shown that this approximation leads to sufficient accuracy for scatter estimation [43].

Fig 7 illustrates the coordinate system and the breast projections on the detector. The semi-ellipse outlined in grey represents the projection after the logarithmic operation (i.e., the line integrals) of the modelled breast in MC simulation. The center of mass (COM) projected on to the detector is denoted as point $O(u_0, v_0)$. The region in dashed line represents the clinical research CBBCT projection acquired on a patient after the logarithmic operation, with the COM at point $O'(u_t, v_t)$. Note that the chest wall region is segmented and removed from the image, and therefore is not used in the COM calculation.

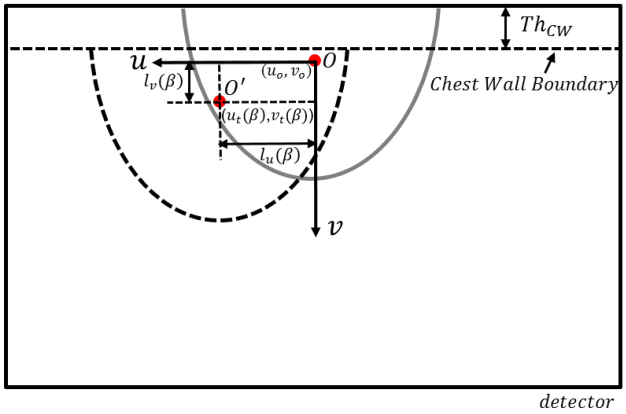

Fig 7 CBBCT projection coordinate system for describing the spatial translation of $S_{D_{eff}}(u, v)$.

To obtain the scatter distribution at each projection angle β, for correction on the clinical data, $\hat{S}(u, v, \beta)$, we spatially shift the scatter distribution $S_{D_{eff}}(u, v)$ selected from the library by the distance between the COMs calculated for each projection angle β, i.e.:

$$\hat{S}(u, v, \beta) = S_{D_{eff}}(u - l_u(\beta), v - l_v(\beta)) \tag{2}$$

The shifting distance along the lateral and longitudinal directions, l_u and l_v, are calculated as:

$$l_u(\beta) = u_t(\beta) - u_0 \tag{3}$$

$$l_v(\beta) = v_t(\beta) - v_0 = Th_{CW} \tag{4}$$

where Th_{CW} is the thickness of the chest wall. Note that, the COM of the breast projection varies for different projection angles β, leading to a β-dependent l_u. Th_{CW} typically remains unchanged for different projections, and thus l_v is constant over different β. When

the translated coordinate $(u - l_u(\beta), v - l_v(\beta))$ is outside the domain of the scatter distribution stored in the scatter library, pixel values are obtained via extrapolation.

The obtained scatter distribution, $\hat{S}\ (u, v, \beta)$, needs to be multiplied by a conversion ratio, $k(\beta)$, to match the magnitude or the unit of scatter signals in a patient scan. This ratio can be calculated by comparing the total signal levels of the raw projection data before the logarithmic operation in a simulated projection and in a patient projection. Denote the raw projection on a patient as $T\ (u, v, \beta)$, which contains both primary and scatter signals, and one obtains the conversion ratio for each projection angle as:

$$k(\beta) = \frac{\sum_{(u,v)\in\Omega} T(u, v, \beta)}{\sum_{(u,v)\in\Omega}\left[\hat{P}(u, v, \beta) + \hat{S}(u, v, \beta)\right]} \tag{5}$$

where $\hat{P}$ is the primary distribution obtained via translating the original simulated primary signals in the same way as the calculation of $\hat{S}$ from $S_{D_{eff}}$. To increase the estimation accuracy, we calculate the conversion ratio using pixels only inside the projected breast on the detector, defined as a region of interest (ROI), Ω, in Eqn. (5).

To prevent overcorrection of scatter, which results in negative values of estimated primary signals, we apply a softcut function, f, on the scatter estimate after magnitude conversion to obtain the final scatter estimate. The softcut function ensures that the estimated scatter is always less than the measured projection data. If the estimated scatter is larger than a user-defined threshold, which is close to but smaller than the measured raw projection, an empirical exponential function is applied to limit the output value below the

measured raw projection. Details of the softcut function can be found in Ref.[64]. The scatter corrected projection data are finally obtained as:

$$T_e(u,v,\beta) = T(u,v,\beta) - f(\, k(\beta) \cdot \hat{S}(u,v,\beta)\,) \tag{6}$$

2.2.3 Summary of the work flow

Fig 8 summarizes the workflow of the proposed library-based scatter correction algorithm as the following steps:

Step 1: Reconstruct first-pass CBBCT images using uncorrected raw projection data.

Step 2: Determine the chest wall boundary from CBBCT projection and then locate its corresponding coronal slice from the first-pass reconstructed image acquired in Step 1.

Step 3: Determine the D_{eff} from the selected slice using Eqn. (1).

Step 4: Select the proper $S_{D_{eff}}(u,v)$ from MC scatter library according to D_{eff}.

Step 5: For each projection view, perform spatial translation on $S_{D_{eff}}(u,v)$ via Eqns. (2-4), adjust magnitude by multiplying the factor calculated via Eqn. (5), and apply the softcut function to obtain the scatter estimate.

Step 6: Subtract the scatter estimate from the measured CBBCT projection to obtain the scatter corrected projection using Eqn. (6).

Step 7: Reconstruct to obtain scatter-corrected CBBCT images.

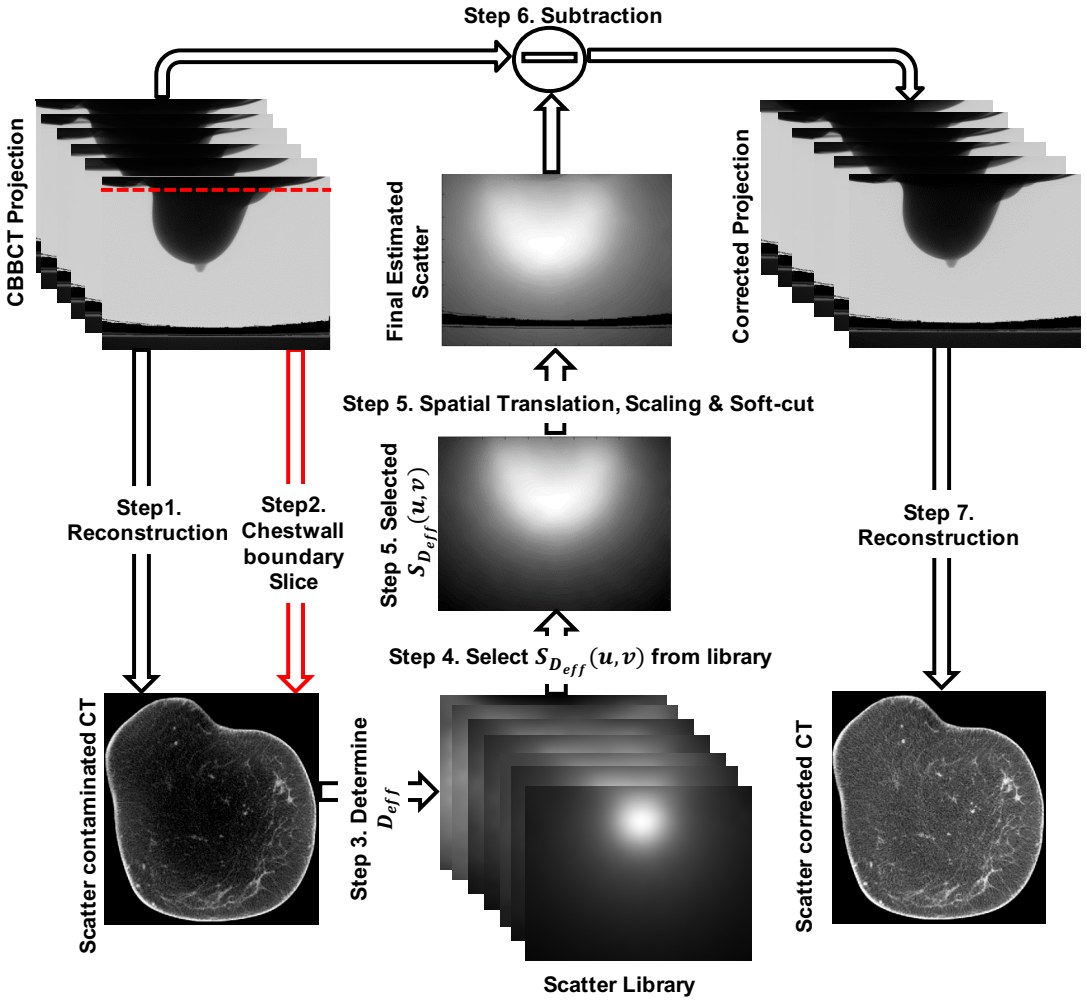

Fig 8 Flowchart of the proposed library-based scatter correction.

2.2.4 Evaluation

2.2.4.1 Validation of Monte Carlo Simulation

We first use a large number of photons (7×10^7 photons per energy bin) in the MC simulation to generate scatter distributions with low noise levels. Based on Poisson statistics, we estimate the average statistical precision (i.e. uncertainty) as 4.47% for a breast with a 14-cm diameter and 4.87% for a large breast with an 18-cm diameter. These results are considered as the ground truths. To shorten the computational time, we generate our library using reduced number of photon (1.2×10^7 photons per energy bin) and a surface fitting algorithm (i.e., Gridfit), as discussed in section 2.2.2.1. The resulting scatter distributions are compared with the ground truths for validation.

2.2.4.2 Patient Evaluation

We demonstrate the feasibility and evaluate the performance of the proposed library-based scatter correction via a retrospective study with 15 clinical research patient datasets. These patient data were from a clinical study which was conducted in accordance with a protocol that was approved by the institutional review boards of the University of Rochester Medical Center and the University of Massachusetts Medical School. All these cases were highly suspicious for malignancy and were assigned category 4 or 5 according to the Breast Imaging-Reporting and Data System (BI-RADS) of the American College of Radiology (ACR) [84].

The clinical research CBBCT prototype system (Koning Corporation, West Henrietta, NY, USA) use a 49 kVp tungsten anode spectrum with a first half-value layer

of 1.39 mm Al and a mean energy of 30.4 keV[85]. The tungsten target x-ray tube (RAD71SP, Varian Medical Systems, Salt Lake City, UT) is powered by a high frequency generator (Sedecal, USA) and the detector is a thallium-doped Cesium Iodine (CsI:Tl) flat-panel detector(PaxScan® 4030CB, Varian Medical Systems, Salt Lake City, UT). Each CBBCT scan acquires 300 projections over 360 degrees, each with a size of 1024-by-768 pixels. The reconstructed CBBCT images have an isotropic voxel size of 0.273 mm. Except for the generation of the scatter library via MC simulation all other steps of our method are implemented in Matlab. The standard FDK reconstruction is implemented using graphics processing unit (GPU) acceleration. On a 1.6 GHz 64-bit windows 7 workstation with NVIDIA Quadro 620 GPU, it takes an average of 3.5 minutes to reconstruct the volumetric CBBCT images with a typical size of 1024-by-1024-by-450. The time for reconstruction slightly varies depending on the breast length along the y direction. The other processing steps to generate scatter-corrected projections (including library selection, spatial translation and soft-cut) currently do not use the GPU-based parallel computing and take about 1 min total for each patient dataset.

One focus of our evaluation studies is to investigate the effects of the simple breast model on the efficacy of scatter correction, and to optimize the method parameters. No beam hardening correction has been implemented. In particular, we aim to find out: 1) whether ignoring the chest wall in the generation of scatter library results in significant errors in scatter correction; 2) whether breast size and VGF, the two parameters used in typical MC studies of breast imaging [73],[75],[77],[86] are both needed as the input parameters of the scatter library; 3) what precision is required on the input parameter(s) of the scatter library.

2.2.4.2.1 *Chest Wall Effect*

For generality of the scatter library and computation simplicity, we do not include the chest wall in the MC simulations for generating the scatter library. To investigate if the presence of chest-wall in clinical data affects the scatter correction performance, additional MC simulations are conducted with the chest-wall modelled as a cylinder of 2 cm height and 28 cm diameter, corresponding to the maximum scanner field-of-view. We compare the scatter corrected images of two patient cases (D_{eff} =14 and 18 cm) using the scatter distribution obtained with and without the chest wall in MC simulation.

2.2.4.2.2 *Effect of Volumetric Glandular Fraction*

A previous study showed that the distribution of scatter-to-primary ratio (SPR) is minimally affected by different values of VGF in breast CT imaging [39]. Since CT image error in the presence of scatter is a function of SPR[87], we hypothesize that the scatter correction performance of the proposed library-based method is insensitive to VGF values, and VGF can therefore be fixed in all MC simulations.

To verify our hypothesis, we compare the scatter-corrected images on one patient using the library-based method with different VGF values (2%, 15%, 35%, 50%, and 75%) in the generation of the scatter library using MC simulation. The patient has a true VGF value of 15%, which is estimated from the first-pass reconstructed images by using a Gaussian-kernel based Fuzzy C-mean (KFCM) algorithm that had been previously published[79].

2.2.4.2.3 Effect of Breast Size

The breast diameter, D_{eff}, has the largest effect on the scatter correction result using our method. The breast diameters from 10 to 18 cm represent 95% of general population in the United States[77], with an average of 14 cm[73]. We therefore use a D_{eff} range of 6 to 22 cm for generating the scatter library. To investigate the required precision of D_{eff} for accurate scatter estimation, we compare the scatter correction results on the same patient using different D_{eff} values with an interval of 2 cm. To investigate the impact of breast length, L_{eff}, MC simulations are performed with varying L_{eff} (0.5, 0.75 and 1.0 times the D_{eff}). The resultant scatter distributions are used for scatter correction on the same patient for comparison.

2.2.4.2.4 Test of Method Robustness and Image Quality Metrics

We test the robustness of our method with 15 clinical research patient datasets. The focus is to evaluate the performance of the scatter correction method on patient datasets that included large variations in breast sizes and VGF, and irregular breast shapes.

In all of the evaluation studies, we use spatial non-uniformity (SNU) and contrast to signal deviation ratio (CDR) as quantitative metrics. The SNU is calculated using five selected ROIs randomly distributed in the adipose tissue area on the reconstructed image:

$$SNU = (\bar{\mu}_{max} - \bar{\mu}_{min})/\bar{\mu}_{mean} \quad (7)$$

where $\bar{\mu}_{max}$ and $\bar{\mu}_{min}$ are the maximum and the minimum of the mean CT values of the selected ROIs, respectively, and $\bar{\mu}_{mean}$ is the average of the mean CT values of the ROIs. The SNU well quantifies the global cupping artifacts on the CBBCT images.

To compute the CDR, we first segment glandular and adipose tissues on the reconstructed image using the KFCM segmentation method [79]. The image contrast is defined as the mean signal difference between the attenuation coefficients of the glandular and adipose tissues, and the CDR is calculated as:

$$CDR = \frac{\bar{\mu}_g - \bar{\mu}_a}{\sigma_a} \tag{8}$$

where $\bar{\mu}_g$ and $\bar{\mu}_a$ are the mean attenuation coefficients of the segmented glandular and adipose tissues, respectively. σ_a is the signal standard deviation measured on the segmented adipose tissue. Fig 9 illustrates the above procedures of CDR calculation. We calculate image contrast in a conventional way as the mean signal difference between adipose and glandular tissues. Since we investigate our method performance on clinical images, it is difficult to select an absolutely uniform area and then measure the image noise. σ_a in Eqn. (8) is different from the statistical image noise, and it actually includes two more terms, image non-uniformity due to existing image artifacts and small background structures. Readers should be aware that our definition of CDR is different from that of the contrast-to-noise ratio (CNR).

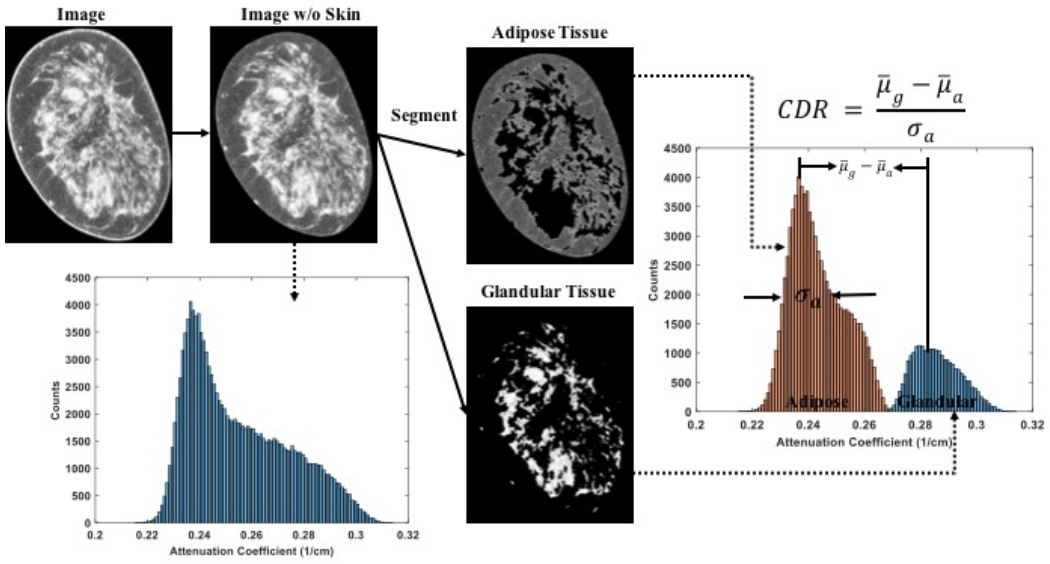

Fig 9 Illustration of the CDR calculation.

2.3 Results

2.3.1 Validation of Monte Carlo Simulation

The computation time of each simulation with a large number of photons (7×10^7 photons per energy bin) takes approximately 21 hours, which is reduced to 3.3 hours (i.e., by a factor of nearly 7) using the proposed method with a reduced number of photons (1.2×10^7 photons per energy bin) and surface fitting. Compared with the ground truth, the scatter distribution obtained by our method has a root-mean-squared difference (RMSD) of 0.04% for a 14 cm diameter breast and 0.08% for a large 18 cm diameter breast. This result has been reported in our prior work[88].

Fig 10 shows the SPR maps inside the breast region on the detector for different breast diameters D_{eff}, along with the comparison of their central column profiles in the

chest-wall to nipple direction. These simulated SPR maps are consistent with published results from other research groups [39].

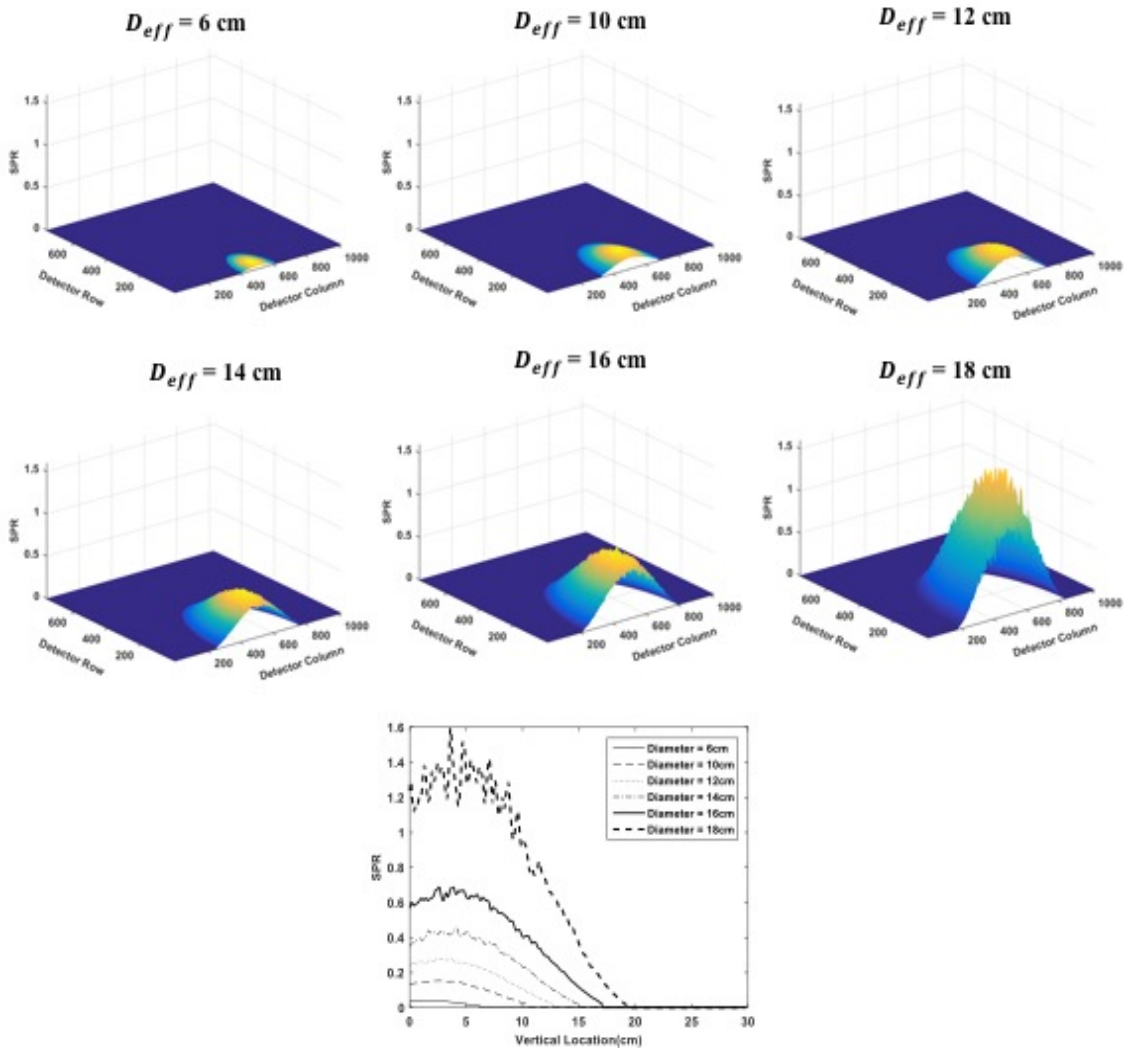

Fig 10 SPR maps for different breast sizes and comparison of the central line profiles in the chest-wall to nipple direction.

2.3.2 Chest-Wall Effect

Two sets of clinical research patient data, one with an average breast (D_{eff}=14 cm, shown in Fig 11 (A) columns (a) and (b)) and the other with a large breast (D_{eff}=18 cm, shown in Fig 11 (A) columns (c) and (d)) are used to investigate the scatter correction

performances when the chest-wall is included or excluded during MC-based generation of the scatter library. Fig 11 compares the images without correction, corrected using the library-based method with and without including the chest wall in the MC simulation, and the difference between the two correction schemes. The proposed library-based correction significantly improves the overall image uniformity and contrast. The extracted 1D profiles taken at the dashed lines shown in the first row of Fig 11 (A) are compared in Fig 12. As shown in the fourth row of Fig 11 (A) as well as in Fig 12, inclusion of the chest wall in the generation of the scatter library leads to negligible difference on the image quality. The RMSD between the scatter-corrected images with and without including the chest wall in the MC simulation is 0.98% and 1.58% for the coronal and sagittal views of the average-size breast, respectively, and 1.09% and 1.96% for the large breast. Most of large differences lie in the area behind the chest wall. Fig 11 (B) shows the same comparison as Fig 11 (A) for a near-chest-wall coronal slice with tissue truncation. The maximum percentage difference and RMSD between the two scatter-corrected images are 3.34% and 0.27% for the average breast, and 5.80% and 1.31% for the large breast, respectively. This study indicates that it is practical to ignore the chest wall during the generation of scatter library for the implementation simplicity of the proposed algorithm without much degradation of scatter correction accuracy.

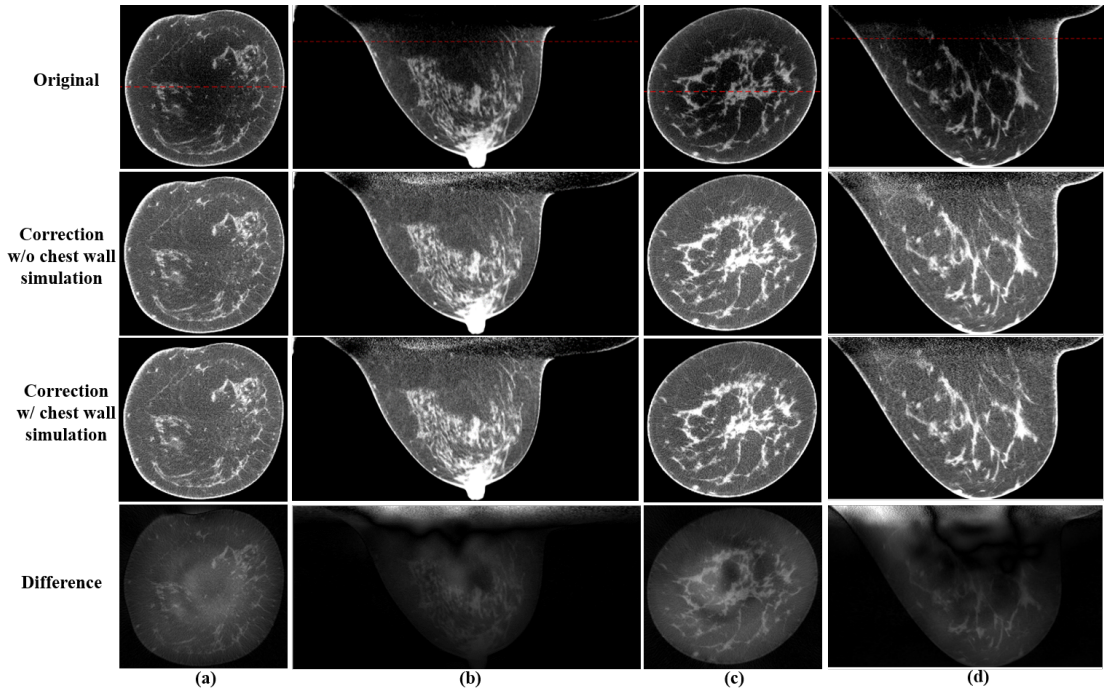

(A)

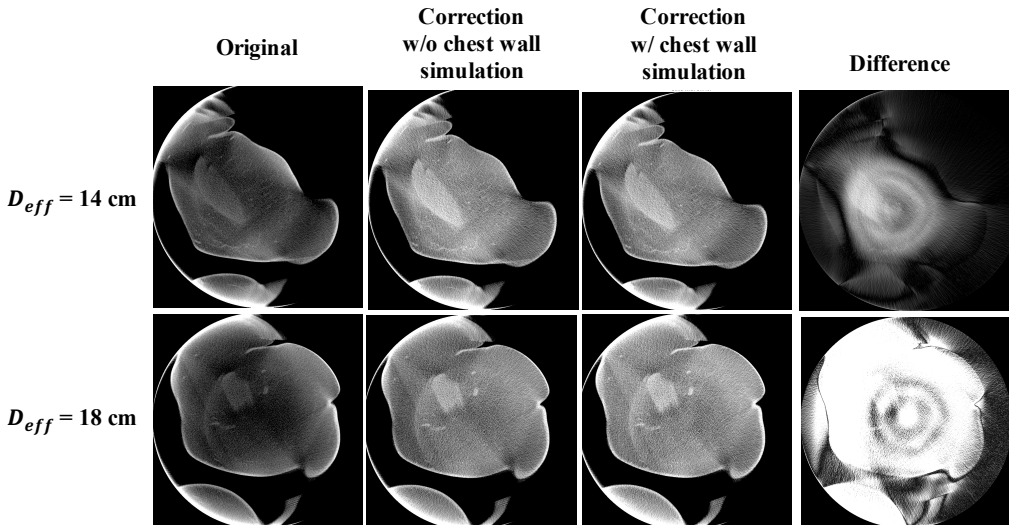

(B)

Fig 11 Demonstration of the chest wall effect in the proposed library-based scatter correction. (A) Comparison of patient images without correction (first row), corrected using the library-based method without and with the inclusion of the chest wall in the MC simulation (second and the third row, respectively), and the difference between the two correction schemes (fourth row). Columns (a) and (b):

Coronal and sagittal views for an average size breast with D_{eff} of 14 cm. Columns (c) and (d): for a large size breast with D_{eff} of 18-cm. Display window:[0.2 0.3] cm^{-1} for the first three rows, [-0.01 0.01] cm^{-1} for the last row. The dashed lines in the first row indicate where the 1D profiles of Fig 11 are taken. (B) Comparison of scatter corrected images near chest wall. Top row shows the results for an average breast size of 14 cm and bottom row for a large breast size of 18 cm. The display windows for uncorrected/corrected images and difference images are the same as those in (A).

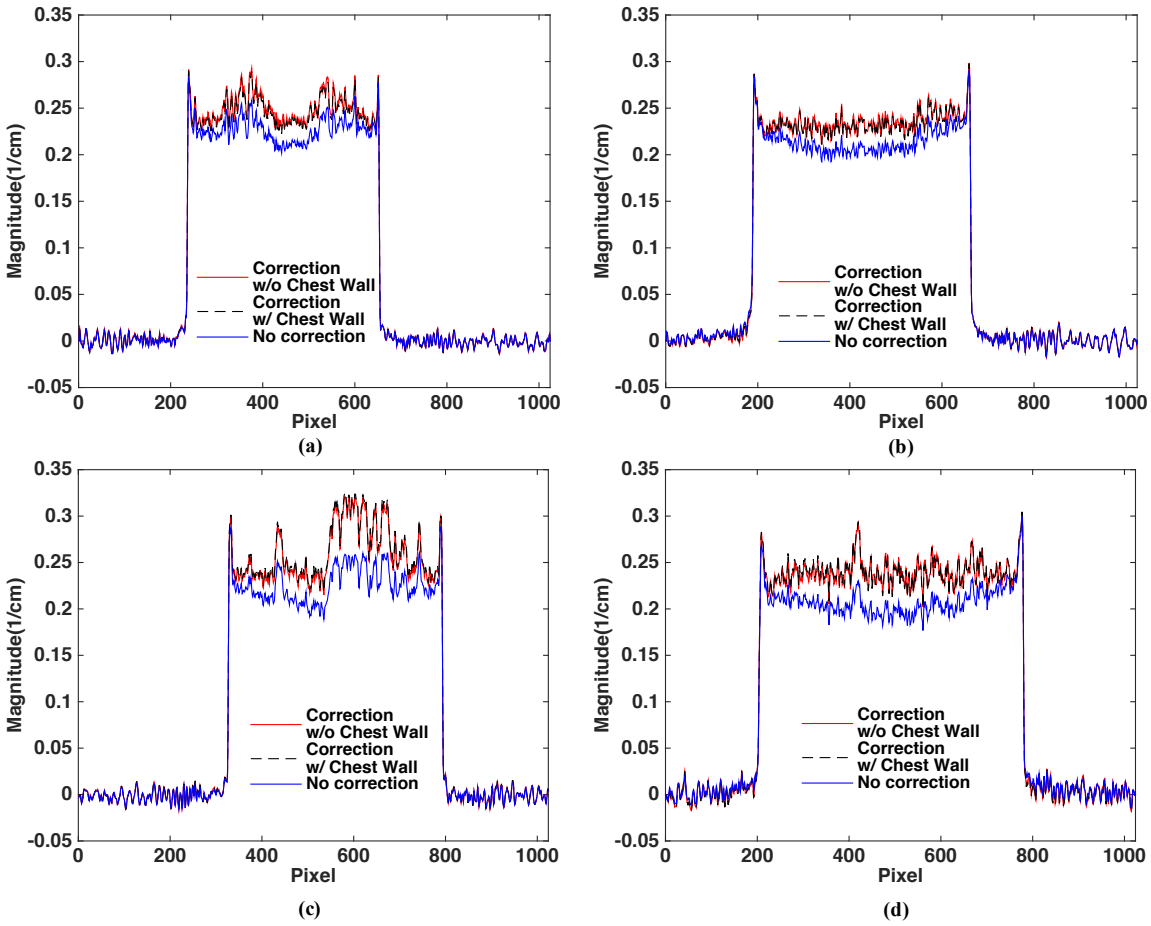

Fig 12 1D profiles taken on the images of Fig 11 (A). The location where the 1D profiles are taken is shown as the dashed lines in the first row of Fig 11 (A).

2.3.3 Effect of VGF

Fig 13 demonstrates the effect of VGF on the performance of our method. The first column of Fig 13 shows the uncorrected image (top row) and the image corrected by the

library-based approach using the true VGF value of 15% (bottom row). The proposed correction greatly improves the image quality. The SNU calculated from the selected ROIs is reduced from 7.70% to 2.50%, and the CDR is improved from 5.48 to 9.26, a nearly two-fold increase. Fig 13 also includes the images corrected by the library-based approach using incorrect VGF of 2%, 35%, 50% and 75%, and their differences compared with the result using the true VGF value of 15% is shown in the bottom row. It is seen that the performance of our method is insensitive to the accuracy of the VGF value. Table 1 summarizes the quantitative analysis on the images of Fig 13. Although the correction result using the true VGF value has the best (lowest) image SNU and high CDR, the error on the VGF value results in very small differences on the image quality. Even with an inaccurate VGF value of 75%, the image SNU is degraded by less than 0.8% and the image CDR is reduced by less than 4%. The above comparison indicates that the performance of the library-based scatter correction is minimally affected by the VGF. Hence, we fix the VGF at 15% in all subsequent implementations presented in this work. During MC simulation for the scatter library generation, this scheme reduces the library size and therefore the computation burden.

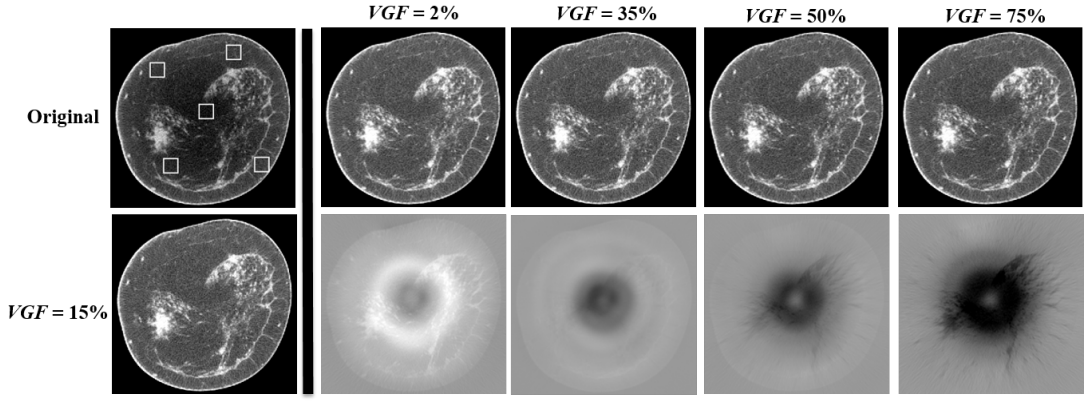

Fig 13 Demonstration of the effect of different VGF values on the performance of the library-based scatter correction. The first column shows the uncorrected original image (upper) and corrected image(bottom) using the true VGF value of 15%. The rest of upper row: image corrected using different VGF values. Display window: [0.2 0.3] cm^{-1}. The rest of bottom row: difference images compared with the result using a VGF value of 15%. Display window: [-0.003 0.002] cm^{-1}. The five white squared ROIs defined in the uncorrected image are used to calculate the SNU values shown in Table 1.

Table 1 Comparison of SNU, CDR and CDR increase ratio on the uncorrected and the corrected images using different VGF values.

	No Correction	Correction with different VGF values				
		2%	15%	35%	50%	75%
SNU(%)	7.70	2.79	2.52	3.21	3.13	3.28
CDR	5.48	9.38	9.26	9.19	9.09	8.89
CDR Increase Ratio	1.00	1.71	1.69	1.68	1.66	1.62

2.3.4 Effect of Effective Breast Diameter (D_{eff}) and Breast Length (L_{eff})

We use one randomly selected breast to investigate the effect of D_{eff} on the correction performance of the proposed method. Based on Eqn. (1), the breast has a measured D_{eff} of 14.1 cm. We therefore use 14 cm as the "true" D_{eff} in the proposed library-based scatter correction. The first column of Fig 14 (A) shows the uncorrected image and the image corrected by the library-based method using the "true" D_{eff} value. The L_{eff} used for this evaluation is fixed at $0.75 \cdot D_{eff}$. The rest of Fig 14 (A) are the images corrected by the library-based method using different D_{eff} values (6, 10, 12, 16, 18, 22 cm; top row) and their corresponding difference compared to the result using the "true" D_{eff} (bottom row). The quantitative analysis of the uncorrected and the corrected images is summarized in Table 2. The D_{eff} has a larger effect on the scatter correction

performance for our algorithm than the VGF. In general, using a D_{eff} smaller (or larger) than the estimated value leads to under (or over) correction of scatter with the proposed algorithm. As shown in their corresponding difference compared to the result using the "true" D_{eff} (bottom row). The quantitative analysis of the uncorrected and the corrected images is summarized in Table 3, a D_{eff} estimated using Eqn. (1) indeed achieves an optimal image quality with both low SNU and high CDR. It is worth noting that the results around the "true" D_{eff} values (i.e., using D_{eff} values of 12 cm, 14 cm and 16 cm) have small differences in these metrics. This finding indicates that the scatter library does not need high precision of D_{eff} for the success of our method. We therefore propose to pre-compute the scatter library using breast models with D_{eff} in 2 cm intervals.

The same patient data are used to investigate the effect of L_{eff} on the scatter correction performance. By fixing the D_{eff} at the "true" value of 14 cm, we carry out scatter correction using scatter maps generated with L_{eff} equal to $0.5 \cdot D_{eff}$ and $1 \cdot D_{eff}$. The first column of Fig 14 (B) shows the uncorrected image and the image corrected using a scatter map with L_{eff} of $0.75 \cdot D_{eff}$. The rest two columns of Fig 14 (B) are the images corrected using scatter maps with L_{eff} of $0.5 \cdot D_{eff}$ and $1 \cdot D_{eff}$, and their corresponding differences compared to the result using $0.75 \cdot D_{eff}$. The quantitative comparison, Table 3, shows that the discrepancy between corrected images using different L_{eff} values is less than 0.7% on SNU and is less than 5.6% on CDR. This finding indicates that the L_{eff} has a small effect on the proposed method. Therefore, it is practical to fix the L_{eff} at $0.75 \cdot D_{eff}$ during the MC simulation for better computation efficiency.

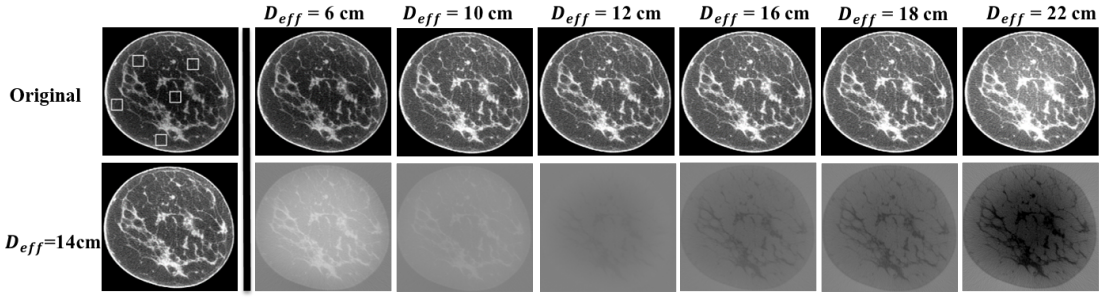

(A)

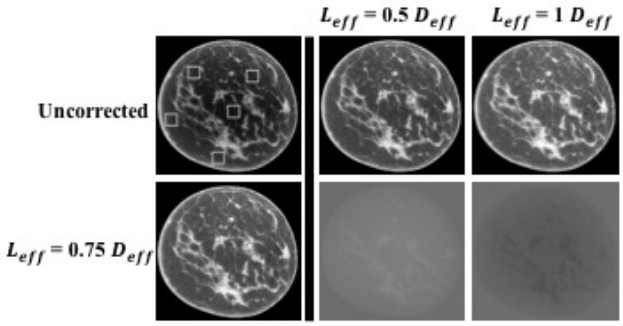

(B)

Fig 14 Demonstration of the effect of different D_{eff} and L_{eff} values on the performance of the library-based scatter correction. (A) The scatter correction results using different D_{eff} values. The first column shows the uncorrected image (upper) and the corrected image (bottom) using an estimated D_{eff} of 14 cm. The rest of upper row: image corrected using different D_{eff} values. Display window: [0.2 0.3] cm^{-1}. The rest of bottom row: difference images compared with the result using a D_{eff} value of 14 cm. Display window: [-0.03 0.04] cm^{-1}. (B) The scatter correction results using different L_{eff} value. The first column shows the uncorrected image (upper) and the corrected image (bottom) using an estimated L_{eff} of $0.75\ D_{eff}$. The rest of the upper row: images correted with $L_{eff}\ of\ 0.5\ D_{eff}$ and $1 D_{eff}$. the bottom row: the corresponding difference images compared with result using a L_{eff} of $0.75\ D_{eff}$. The diasplay windows for uncorrected/corrected images and difference images are the same as those in (A).

Table 2 Comparison of SNU, CDR and CDR increase ratio on the uncorrected image and the corrected images using different D_{eff} values.

	No Correction	Correction with different D_{eff} values						
		6cm	10cm	12cm	14cm	16cm	18cm	22cm
SNU(%)	6.30	4.25	2.26	1.77	1.79	2.07	2.58	7.40
CDR	5.36	5.70	5.94	5.81	5.95	5.76	5.69	4.92
CDR Increase Ratio	1.00	1.06	1.11	1.08	1.11	1.08	1.06	0.92

Table 3 Comparison of SNU, CDR and CDR increase ratio on the uncorrected image and the corrected images using different L_{eff} values.

	No Correction	Correction with different L_{eff} values		
		0.50*D_{eff}	0.75*D_{eff}	1.00*D_{eff}
SNU(%)	6.302	1.806	1.789	2.408
CDR	5.358	5.598	5.937	5.942
CDR Increase Ratio	1.000	1.045	1.108	1.109

2.3.5 Patient Group Study

To demonstrate the efficacy and robustness of the proposed method, Table 4 summarizes the results on 15 breast patients. For all the cases, we compare the SNU and CDR in both coronal and sagittal views without and with scatter correction. For coronal views, the proposed method improves the CDR on average by a factor of 1.49 and the SNU is reduced from 7.14% to 2.47%, on average. Similar performance is also observed in

sagittal views, where the CDR is improved on average by a factor of 2.12 and the SNU is reduced from 10.14% to 3.02%, on average.

To scrutinize the method performance, we compare the library-based scatter correction method with two other correction methods: constant correction and system correction. In the constant correction method, we assume that scatter has a uniform distribution and scatter correction is carried out by subtracting a constant value from the measured projection. The constant, i.e., the scatter level, is estimated from the simulated SPR (shown in Fig 10) according to the breast size and fixed as 75% of the maximum scatter signal for a balanced performance for all patient cases. The system correction method is an algorithm embedded in the imaging software of the commercial CBBCT scanner which we use to acquire all the patient data. In Fig 15, we show representative results on three patient cases, and a comparison of image SNU is listed in Table 5. It is found that only the library-based approach stably removes the shading artifacts and obtains corrected images with low SNU for all patient cases. The soft tissue abnormalities (indicated by white arrows on patient #1) and calcification clusters (indicated by white arrows on patient #12) become more discernible after the proposed scatter correction. The other two correction methods have unpredictable inferior performances with either scatter overestimation or underestimation.

To further demonstrate the reliability of the library-based scatter correction, Fig 16 shows the correction results for patients with different breast sizes (i.e., D_{eff}) and shapes. It is seen that our method robustly corrects for scatter on CBBCT for a large range of breast diameters from 10 cm to 18 cm.

Table 4 Comparison of SNU, CDR and CDR increase ratio on the 15 patient CBBCT datasets without and with scatter correction. Note that, the VGF values, estimated via the KFCM method, are listed for reference only. They are not used in the proposed library-based scatter correction.

Patient #	D_{eff} (cm)	VGF (%)	Coronal View (x-z)					Sagittal View (x-y)				
			SNU(%) (Before/After)		CDR (Before/After)		CDR Increase Ratio	SNU (Before/After)		CDR (Before/After)		CDR Increase Ratio
1	14	41	6.43	1.07	5.32	6.77	1.27	7.49	2.87	4.28	5.27	1.23
2	14	5	11.92	2.83	2.56	5.48	2.14	14.07	2.12	3.02	8.66	2.86
3	14	18	7.41	3.38	6.76	10.07	1.49	20.18	2.32	1.16	8.52	7.32
4	14	14	6.79	2.70	6.80	9.12	1.34	11.48	3.15	5.01	5.70	1.14
5	14	7	5.66	1.90	5.47	7.50	1.37	6.59	3.34	4.71	7.17	1.52
6	14	16	7.89	2.99	4.06	5.93	1.46	11.74	3.09	3.72	6.31	1.70
7	14	13	13.03	3.30	4.91	6.44	1.31	8.64	2.17	6.56	7.65	1.17
8	14	34	5.24	3.10	5.23	7.35	1.41	9.38	2.98	4.60	6.28	1.36
9	12	15	5.19	2.15	5.17	7.36	1.42	11.02	1.55	4.92	7.74	1.57
10	18	12	12.62	2.82	2.45	6.69	2.73	16.18	6.89	2.38	5.97	2.51
11	10	7	5.20	1.93	9.47	12.94	1.37	9.73	2.13	5.11	9.42	1.84
12	10	1	2.96	1.92	5.08	6.72	1.32	5.60	4.79	4.72	6.53	1.38
13	14	19	4.35	1.70	7.51	9.60	1.28	9.81	2.18	4.73	7.61	1.61
14	10	15	6.65	3.23	6.14	6.18	1.01	4.42	2.72	6.93	7.71	1.11
15	16	21	5.78	1.96	6.43	9.21	1.43	5.84	3.07	1.88	6.58	3.50
Average			7.14	2.47	5.56	7.82	1.49	10.14	3.02	4.25	7.14	2.12
STD			2.94	0.68			0.40	4.10	1.26			1.54

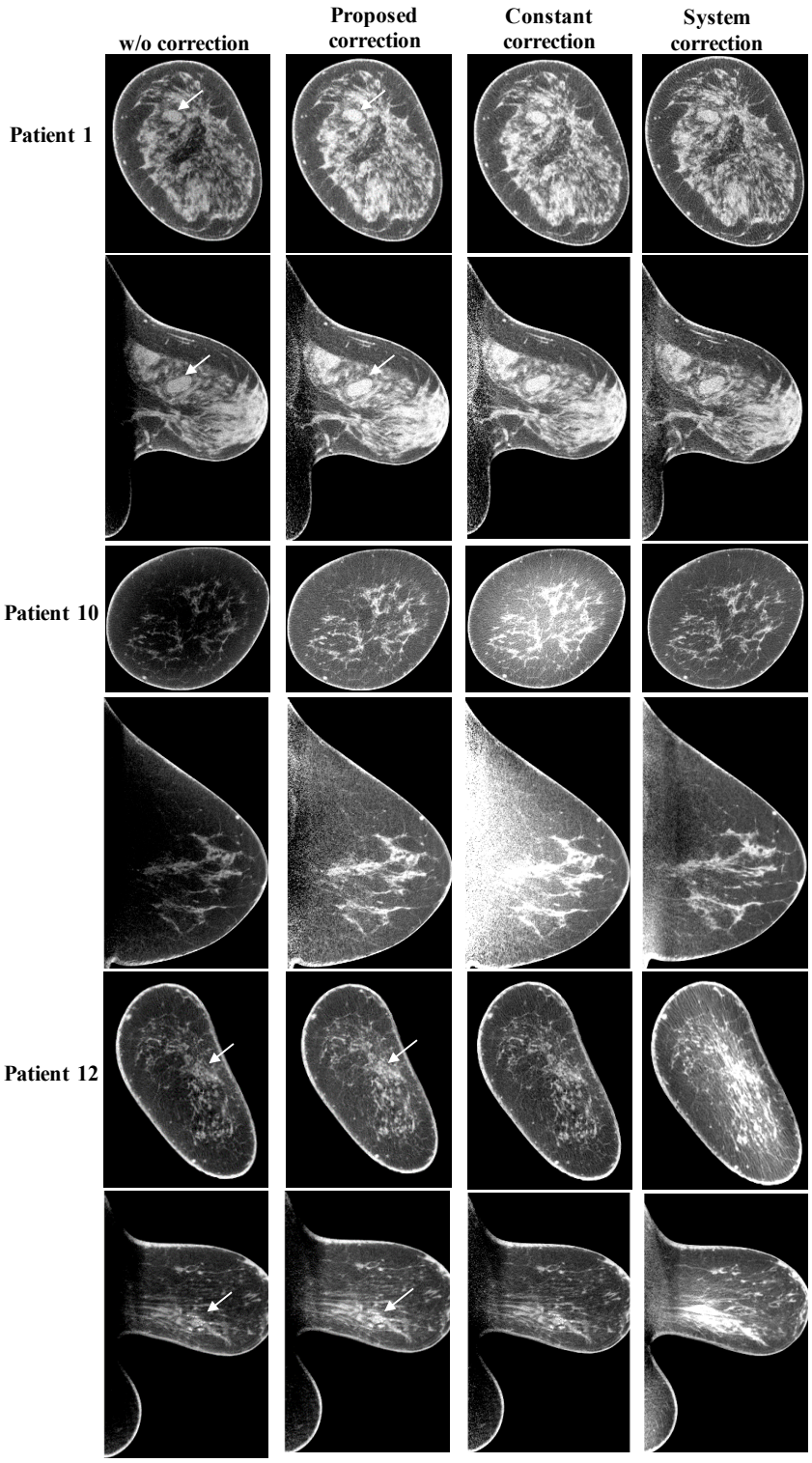

Fig 15 Comparison of typical correction results using the proposed library-based method, the constant correction method, and the software-embedded method (system correction). The lesions are indicated by the white arrows. Display window:[0.2 0.3] cm^{-1}.

Table 5 Comparison of SNU using different scatter correction methods for coronal and sagittal views shown in Fig 15.

Patient #	Coronal View (x-z) SNU(%)			Sagittal View (x-y) SNU(%)		
	Proposed Correction	Constant Correction	System Correction	Proposed Correction	Constant Correction	System Correction
1	1.11	1.56	1.31	2.54	3.70	6.24
10	2.64	11.61	2.29	5.26	28.65	7.85
12	2.53	3.61	7.64	4.79	6.37	9.79

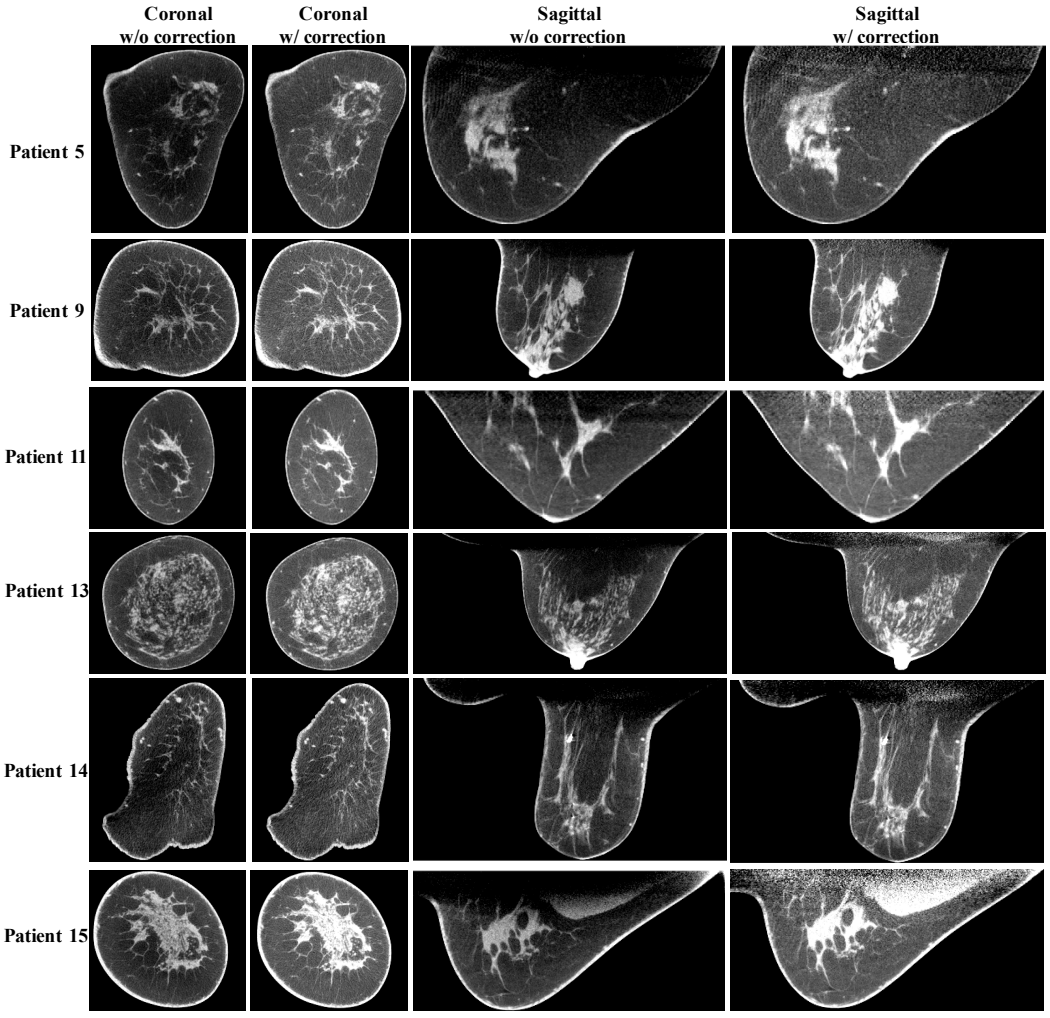

Fig 16 The correction results for breasts with different sizes and shapes . Display window: [0.2 0.3] cm^{-1}.

2.4 Conclusions

In this work, we propose a highly efficient and effective scatter correction method for CBBCT imaging by estimating the scatter based on a pre-computed scatter library using MC simulations. The method performance has been demonstrated on a group of 15 patient datasets acquired from a clinical research CBBCT prototype system. The proposed method effectively reduces the image SNU from 7.14% to 2.47% in the selected ROIs and improves the CDR by a factor of about 1.8 on average. Increased visibility has been observed for soft tissue lesions and calcification clusters, two important indications for breast cancers.

The proposed library-based scatter correction has the following attractive features. First, our method requires no change of the imaging protocol (i.e., no scan time or dose increase) or the system hardware, and therefore can be used as software plug-in in the signal processing chain of current CBBCT systems. Second, due to the simplicity of the CBBCT imaging geometry, we substantially minimize the size of the scatter library without degradation of the method performance, which improves the method practicality by reducing the computation complexity and memory consumption. Third, as the scatter library is pre-computed and stored in a system calibration stage, the scatter correction step is efficiently performed on the real patient data (200 ms per projection in our Matlab implementations). These combined advantages together with the high effectiveness and robustness as demonstrated on patient studies make LB method distinct from the existing scatter correction approaches. By developing an effective yet practical scatter correction method, our research potentially promotes the clinical role of dedicated CBBCT.

The performance of the proposed LB scatter correction can be further enhanced by refining the method design, although the results presented on clinical data indicate a small margin of possible improvements. For example, the scatter library is currently generated via MC simulation on a simplified breast model with only one parameter. We can increase the accuracy of scatter estimation by using a sophisticated breast model with more geometric parameters to account for different breast deformations in a clinical scan. The size of scatter library will increase accordingly by including more breast parameters and one parameter of projection angle due to the loss of rotational symmetry. In the MC simulation engine, the current physics model, which includes only basic collisional interactions, can be improved by more realistic modeling of the x-ray source and the detector. For example, Inclusion of the heel effect on the x-ray tube, a dedicated beam shaping filter [89], and a non-ideal energy response curve on the detector in the MC simulation further increases the scatter estimation accuracy. The proposed correction only removes the low-spatial-frequency component of scatter, and the high-frequency statistical noise of scatter is inevitably left in the scatter-corrected image. We will implement a penalized weighted least square method previously designed for scatter correction algorithms [87] together with the library-based method to further enhance the image CDR.

In addition to the above algorithmic advancements on scatter correction, our future research will include statistical validation of the method accuracy and reliability on more patient studies. As another major source of CT imaging errors, beam hardening effect also causes cupping artifacts on CBBCT, as well as streaks around dense objects [90]. We will design and implement beam hardening correction algorithms to reduce the residual artifacts on the images shown. After these studies, we will investigate the improvements in detection

and classification of breast tumors on CBBCT images achieved by our methods, using both human and numerical observers [91] and computer-aided techniques [92-96].

CHAPTER 3. FORWARD-PROJECTION-BASED SCATTER CORRECTION

3.1 Introduction

In this chapter, we propose a new effective and efficient modeling method for scatter correction on CBBCT images with no assumptions on the breast shape and composition. The main idea of this work is inspired by Ref. [44] , where a planning CT (pCT) based scatter correction approach is proposed for reducing scatter artifacts on CBCT images to improve accuracy of radiation therapy treatment. pCT is commonly available in current radiation therapy and therefore can be used as prior patient information. The basic principle of pCT-based scatter correction is to estimate the primary signals of CBCT projections via forward projection of the registered pCT images, which are considered to be of high quality with negligible scatter contamination. Then the low-frequency scatter in CBCT raw projections is obtained by subtracting the estimated primary signals and low-pass filtering. The previously proposed pCT-based correction cannot be directly used for scatter removal in diagnostic CBBCT imaging where pCT is unavailable. In our published studies [44, 97], we find that the pCT-based scatter correction is accurate even in the area where pCT registration has large errors. On the other hand, breast CT images have approximately binary-object (i.e., fibroglandular and adipose tissue) distributions and existing algorithms have achieved accurate binary segmentation on CBBCT images [79]. We therefore propose to first coarsely segment the first-pass uncorrected CBBCT images into binary-object maps and assign the segmented fibroglandular and adipose tissue with the correct attenuation coefficients based on the mean x-ray energy. The modified CBBCT are treated as the prior

images, in lieu of pCT, in our previously developed algorithm toward scatter correction. Primary signals are first estimated via forward projection on the modified CBBCT. To avoid errors caused by inaccurate segmentation, only sparse samples of estimated primary are selected for scatter estimation. A Fourier-Transform based algorithm, referred to as local filtration, is developed to efficiently estimate the global scatter distribution on detector. The scatter corrected images are obtained by removing the estimated scatter distribution from measured projection data. The proposed method is evaluated on six patients with large variation in breast shapes.

3.2 Methods and Materials

3.2.1 First-pass Estimation of Scatter Signals

We first generate the uncorrected CBBCT images from scatter contaminated projections. In all the presented patient studies, an empirical thresholding method is used to coarsely segment the breast region into adipose and fibroglandular tissues. Voxels with values between 0.1 and 0.24 cm^{-1} are considered as adipose tissue and assigned a uniform value of 0.23 cm^{-1}, and voxels with values above 0.24 cm^{-1} are considered as fibroglandular tissue and assigned a uniform value of 0.28 cm^{-1}. The assigned attenuation coefficients (i.e. μ) are empirically tuned based on the calculated effective mean energy (i.e. 30.4 keV) of the x-ray spectrum (49 kVp with a HVL of 1.39 mm Al) used in the clinical CBBCT system. It is critical to set correct μ values for successful scatter correction using the proposed algorithm. Values too high or too low will result in under or over correction of scatter. However, we find that these μ values can be fixed for all the patient studies presented in this work. Therefore, parameter tweaking of μ does not reduce the practicality

of our method. The resultant image is considered as prior CT, on which forward projection via Siddon's ray tracing algorithm[98] is used to simulate primary projections, i.e., scatter-free line integrals. The estimated line integrals are converted to raw projection (in unit of detector count) using x-ray flat field intensity (I_0), which is determined by taking the average value of a 200 × 200 un-attenuated pixel region on the measured projection data. An initial estimate of the scatter distribution, denoted as S_0 hereafter, is finally obtained by subtracting the simulated primary projection in unit of photon numbers from the measured projection.

3.2.2 Removal of Scatter Estimation Errors and Local Filtration

The resulting S_0 includes both low-frequency scatter distribution, denoted as S_t, and the scatter estimation errors, denoted as S_e, stemming mostly from the difference between the prior CT image generated by coarse segmentation and the true scatter-free CBBCT image. To reduce the impact of S_e on estimation of S_t, we aim to use S_0 only in the area, Ω_s, where S_e is expected to be small, and then generate a whole-field estimation of S_t using low-pass filtration and interpolation. Toward this goal, we first obtain Ω_s as the area with positive and smooth S_0, i.e.:

$$\Omega_s = \{(i,j) | |\nabla S_0(i,j)| < T_g,\ S_0(i,j) > 0\}, \tag{9}$$

where (i,j) is the pixel index on the detector, ∇ calculates the image gradient distribution, and T_g is the threshold of the gradient magnitude of S_0, set at 50 detector counts in our studies.

An estimate of the whole-field scatter distribution, $\hat{S}_t$, is obtained via weighted summation of available sparse samples in Ω_s as:

$$\hat{S}_t(i,j) = \frac{\sum_{(s,t)\in\Omega_s} S_0(s,t)\cdot w_\sigma(i-s,j-t)}{\sum_{(s,t)\in\Omega_s} w_\sigma(i-s,j-t)} \tag{10}$$

where the w_σ is the Gaussian smooth kernel defined as:

$$w_\sigma(s,t) = e^{-\frac{(s^2+t^2)}{\sigma^2}} \tag{11}$$

The kernel width σ is set to be 4 pixels in all the presented studies.

The calculation of Eq. (10) is equivalent to signal smoothing inside Ω_s and interpolation outside. To accelerate the computation, we define an indicator function, f, with the same size of the projection image as:

$$f(\mathrm{i},j) = \begin{cases} 1, & \text{if } (i,j) \in \Omega_\mathrm{s} \\ 0, & \text{otherwise} \end{cases} \tag{12}$$

It can be easily verified that Eq. (10) has an equivalent form using convolution:

$$\hat{S}_t(i,j) = \frac{(S_0 \cdot f) ** w_\sigma}{f ** w_\sigma} \tag{13}$$

Eqn. (13) 13can be efficiently implemented via fast Fourier Transform. We refer to the above technique (Eqn. (13)) as local filtration in this work.

$\hat{S}_t$ is finally removed from the CBBCT raw projections for scatter correction.

3.2.3 Workflow

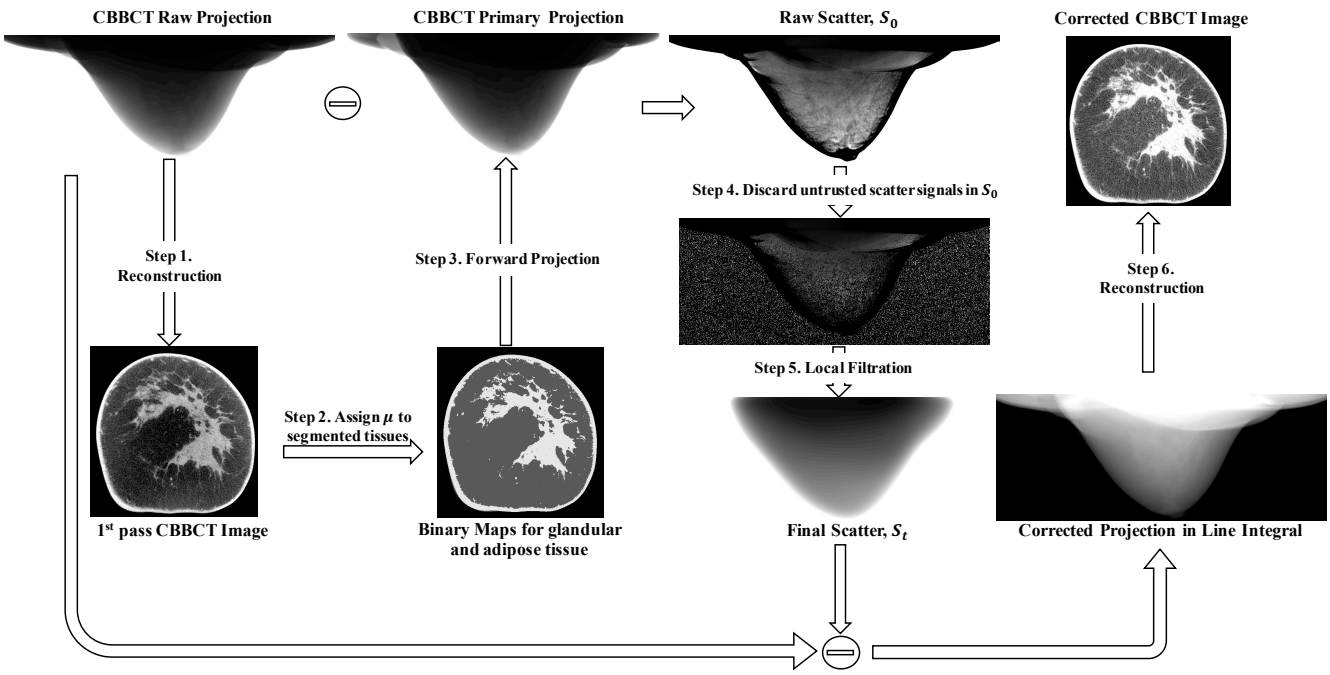

Fig 17 Workflow of scatter correction for CBBCT using the proposed forward projection model.

The workflow of the proposed scatter correction method on CBCT is summarized in Fig 17, with the following steps:

Step 1: Reconstruct the uncorrected CBBCT images using raw projection data.

Step 2: Segment fibroglandular and adipose tissues and assign uniform linear attenuation coefficient values.

Step 3: Forward project the image obtained in *Step 2* to simulate primary projection.

Step 4: Subtract the simulated primary projection from the raw projection to acquire a first-pass scatter estimate, S_0.

Step 5: Obtain sparse samples of S_0 via magnitude and gradient thresholding (Eqn. (9)).

Step 6: Determine the final scatter distribution from the sparse sampled of S_0 in *Step 5* using local filtration (Eqn. (13)). Subtract the final scatter estimate from the raw projection to obtain the scatter corrected projection.

Step 7: Reconstruct to obtain the scatter-corrected CBBCT images.

3.2.4 Evaluation

We evaluate the performance of the proposed scatter correction using a forward projection model on six patients in a retrospective study. These patient data were acquired during a clinical research study under a protocol that was approved by the institutional review boards of the University of Rochester Medical Center and the University of Massachusetts Medical School. The selected six cases were highly suspicious for malignancy and were assigned category 4 or 5 according to the Breast Imaging-Reporting and Data System (BI-RADS) of the ACR.

The clinical research CBBCT prototype system (Koning Corporation, West Henrietta, NY, USA) used for patient data acquisition has a 49 kVp tungsten anode spectrum and a first half-value layer of 1.39 mm Al, which gives a mean energy of 30.4 keV[85]. The tungsten target x-ray tube (RAD71SP, Varian Medical Systems, Salt Lake City, UT) is powered by a high frequency generator (Sedecal, USA) and the detector is a thallium-doped Cesium Iodine (CsI:Tl) flat-panel detector (PaxScan® 4030CB, Varian Medical Systems, Salt Lake City, UT). The source to axis distance (SAD) is 65 cm and the source to detector distance (SDD) is 89.8 cm. Each CBBCT scan acquires 300 projections

over 360 degrees, and each projection has a size of 1024 × 768 pixels. The reconstructed CBBCT images have an isotropic voxel size of 0.273 mm.

In this work, all the data are processed on a 1.6 GHz 64-bit Windows 7 workstation with NVIDIA Quadro 620 GPU. It takes an average of 40 seconds and 3.5 minutes to perform forward-projection and FDK reconstruction, respectively, on a CBBCT volume with a size of 1024 × 1024 × 450. The time for reconstruction slightly varies depending on the breast size. The step of scatter correction in projection domain takes about 10 seconds in total for each patient dataset with 300 projections.

In all of the evaluation studies, we use spatial non-uniformity (SNU) and contrast to deviation ratio (CDR) as image quality metrics[99].

3.3 Results

3.3.1 Scatter Correction on Patient Data

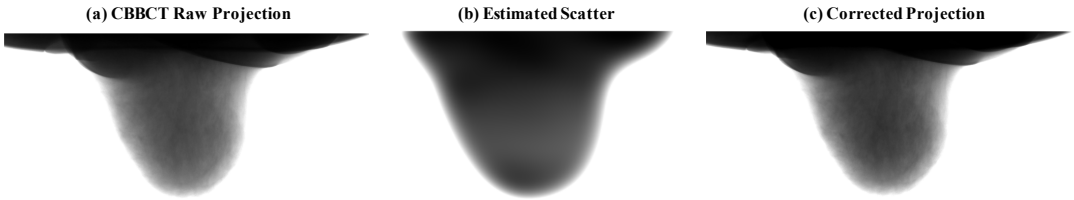

Fig 18 Example of the raw projection, the estimated scatter and the scatter corrected projection. Display window: (a) and (c): [min max], (b) [100 2000] detector counts.

Fig 18 shows one example of the uncorrected and corrected projections and the estimated scatter distribution. Fig 19 compares the uncorrected and the corrected CBBCT images in coronal and sagittal views for four patients. It is observed the proposed method

substantially improve the image quality. For all six patients, the quantitative analysis on both coronal and sagittal views of the uncorrected and the corrected images is summarized in Table 6. For coronal view, the proposed correction reduces the SNU from 8.27% to 1.91% on average and increase the CDR by an average factor of 1.38. For sagittal view, the SNU is reduced from 6.50% to 3.00% on average and the CDR is increased by a factor of 1.44.

Table 6 Comparison of SNU, contrast, σ_a, CDR and CDR increase ratios on the uncorrected image and the corrected images using the proposed method for six patients.

Patient #	Coronal View								
	SNU (%) (Before/After)		Contrast (cm^{-1}) (Before/After)		σ_a (cm^{-1}) (Before/After)		CDR (Before/After)		CDR Increase Ratio
1	9.32	2.45	0.034	0.050	0.010	0.010	3.44	5.00	1.45
2	6.50	1.47	0.045	0.071	0.007	0.009	6.09	7.63	1.25
3	3.89	0.85	0.032	0.046	0.006	0.008	5.17	6.10	1.18
4	7.08	2.06	0.032	0.049	0.007	0.007	4.65	6.88	1.48
5	13.70	3.40	0.035	0.041	0.009	0.009	3.90	4.70	1.21
6	9.10	1.20	0.037	0.066	0.010	0.010	3.80	6.50	1.71
Average	8.27	1.91	0.036	0.054	0.008	0.009	4.51	6.14	1.38
	Sagittal View								
	SNU (%) (Before/After)		Contrast (cm^{-1}) (Before/After)		σ_a (cm^{-1}) (Before/After)		CDR (Before/After)		CDR Increase Ratio
1	8.96	3.96	0.061	0.073	0.031	0.026	2.00	2.79	1.40
2	4.45	3.08	0.041	0.067	0.016	0.017	2.58	4.03	1.56
3	3.35	2.74	0.031	0.045	0.006	0.007	5.41	6.33	1.17
4	6.66	2.90	0.038	0.040	0.010	0.009	3.70	4.44	1.20
5	9.50	3.80	0.039	0.046	0.008	0.009	4.60	5.10	1.11
6	6.10	1.50	0.048	0.070	0.016	0.011	3.00	6.60	2.20
Average	6.50	3.00	0.043	0.057	0.015	0.013	3.55	4.88	1.44

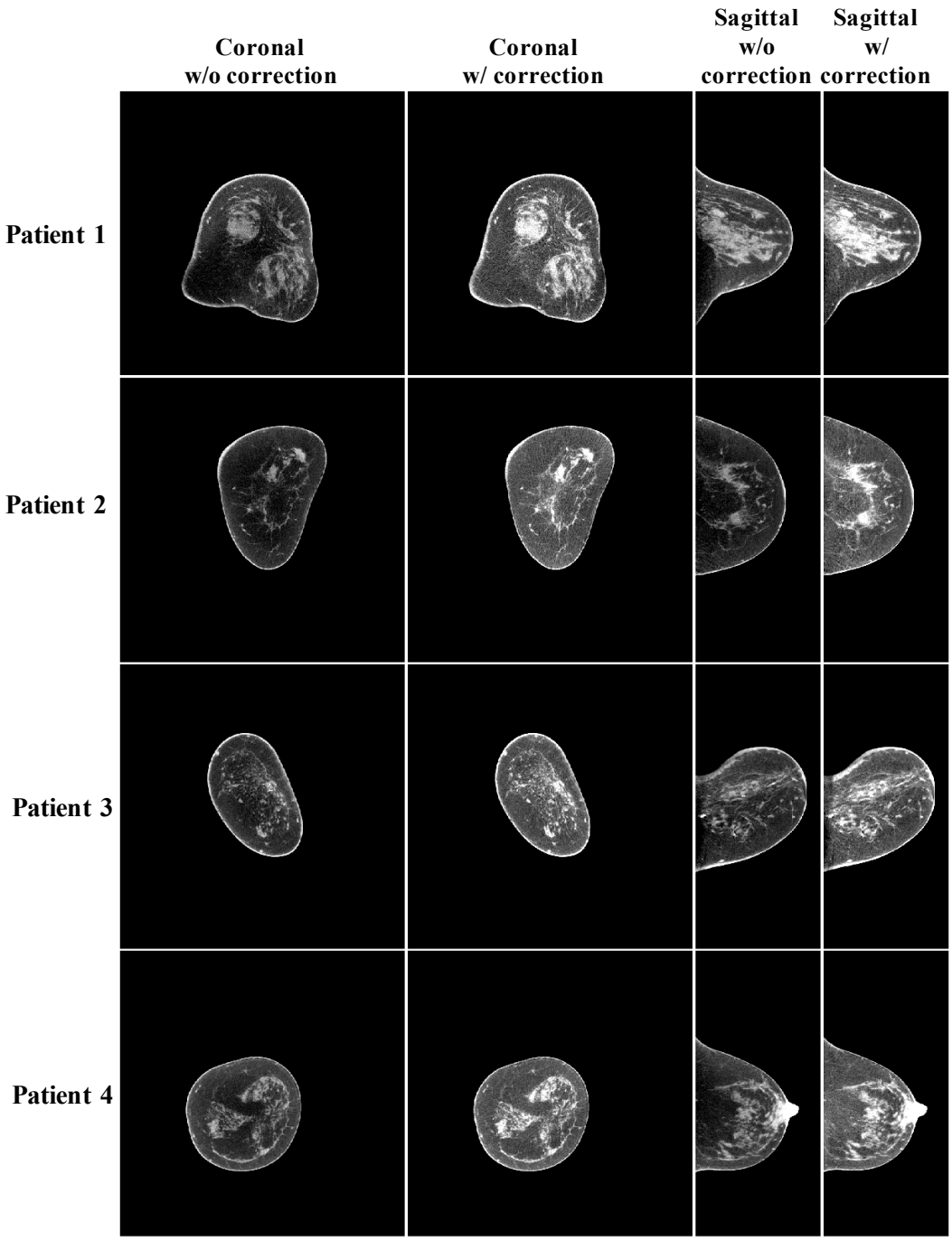

Fig 19 Scatter correction results for four patients with different breast shapes. Display window: [0.2 0.3] cm^{-1}.

3.3.2 Potential Errors Induced by Inaccurate Segmentation

A particular concern regarding the proposed method is that CBBCT generated from coarse segmentation is treated as the prior images and therefore segmentation errors may result in errors for scatter correction. In particular, inaccurate segmentation may potentially alter the anatomical information of CBBCT after scatter correction. Nonetheless, the removal of scatter estimates with large expected errors and the local filtration technique guarantee that the success of the proposed method does not heavily rely on accurate segmentation. To support our argument, we present two more patient studies with large segmentation errors, shown as patient 5 and 6 in Fig 20. In the comparison of the uncorrected image and the image generate via segmentation, it is obvious that the latter loses many fine structures of fibroglandular tissue. After the proposed scatter correction, it is seen that the image uniformities for the two patients are substantially improved without structure alteration (see the comparison of zoom-in images).

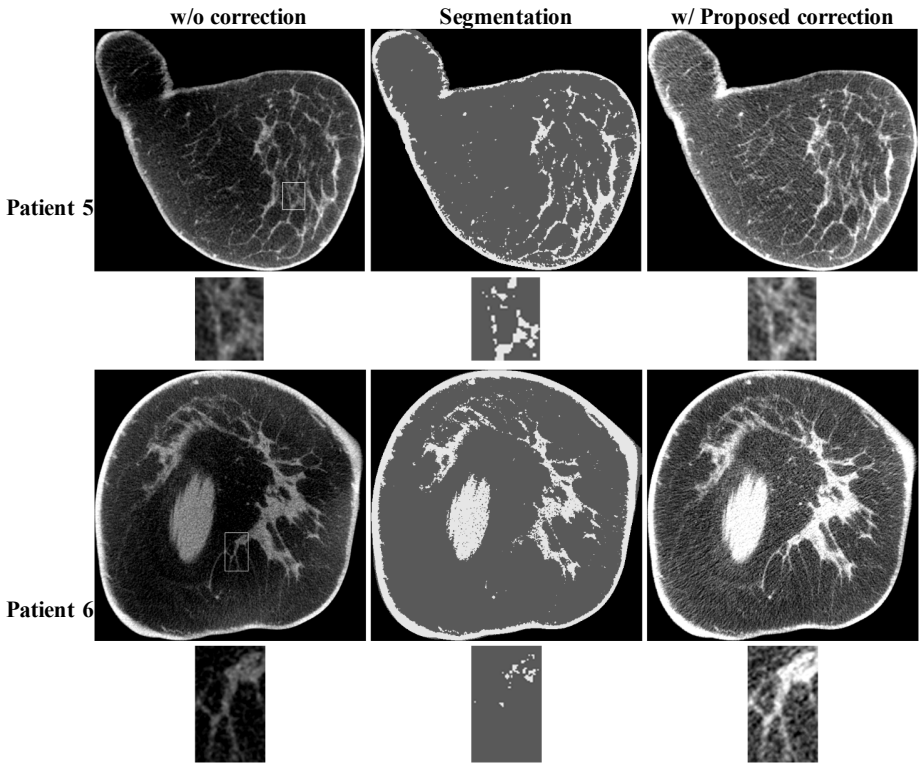

Fig 20 The effect of segmentation errors on the performance of the proposed correction method. For each patient, the images on the top panel are the uncorrected image, the corresponding tissue segmentation and the corrected image using proposed method. The bottom panel shows the zoom-in views of the selected ROI (marked as white squares in the top panel) on the corresponding image above. Display window: [0.2 0.3] cm^{-1}.

3.3.3 Effect of T_g Values on the Method Performance

One merit of the proposed method is that it estimates the whole field scatter distribution using only sparse samples. As shown in Eqn. (9), the gradient threshold, T_g, is the only algorithm parameter in the selection of sparse samples. In this work, we empirically chose a T_g value of 50 detector counts to perform scatter estimation for all the patient cases. To investigate the effect of T_g on the method performance, we compare the corrected images on Patient 6 of Fig. 4 using different T_g values (i.e., 10, 30, 80 and 110) in the proposed algorithm, shown in Fig 21. It is seen that a T_g value either too large or

too small degrades the quality of the resultant image and T_g=50 achieves a minimum image SNU of 2.6%. However, the effect of different T_g values is not obvious on the scatter corrected CBBCT images, and the image SNU remains under 3.0% for a large range of T_g values from 30 to 70.

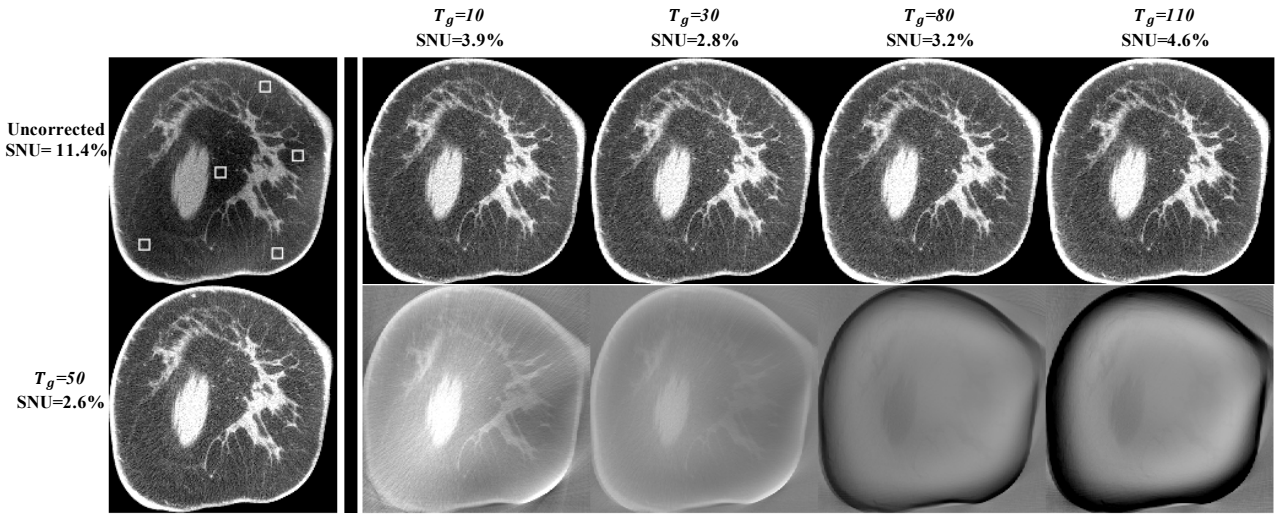

Fig 21 Demonstration of the effect of T_g values on the performance of the proposed method. The first column shows the uncorrected image (upper) and the corrected image(bottom) using T_g =50. The rest of upper row: images corrected using different T_g values. Display window: [0.2 0.3] cm^{-1}. The rest of bottom row: difference images compared with the result using T_g = 50. Display window: [-0.01 0.01] cm^{-1}.

3.3.4 Comparison with the System-embedded Scatter Correction

To further evaluate the performance of proposed method, we compare the corrected images with those corrected by the software embedded on the Koning CBBCT system. Fig 22 shows two representative results of comparison on patient 1 and 3, where scatter correction is particularly challenging due to the irregular breast shapes. Table 7 demonstrates the quantitative comparison of the images in Fig 22. It shows that the proposed method outperforms the system correction in both SNU and CDR increase ratio.

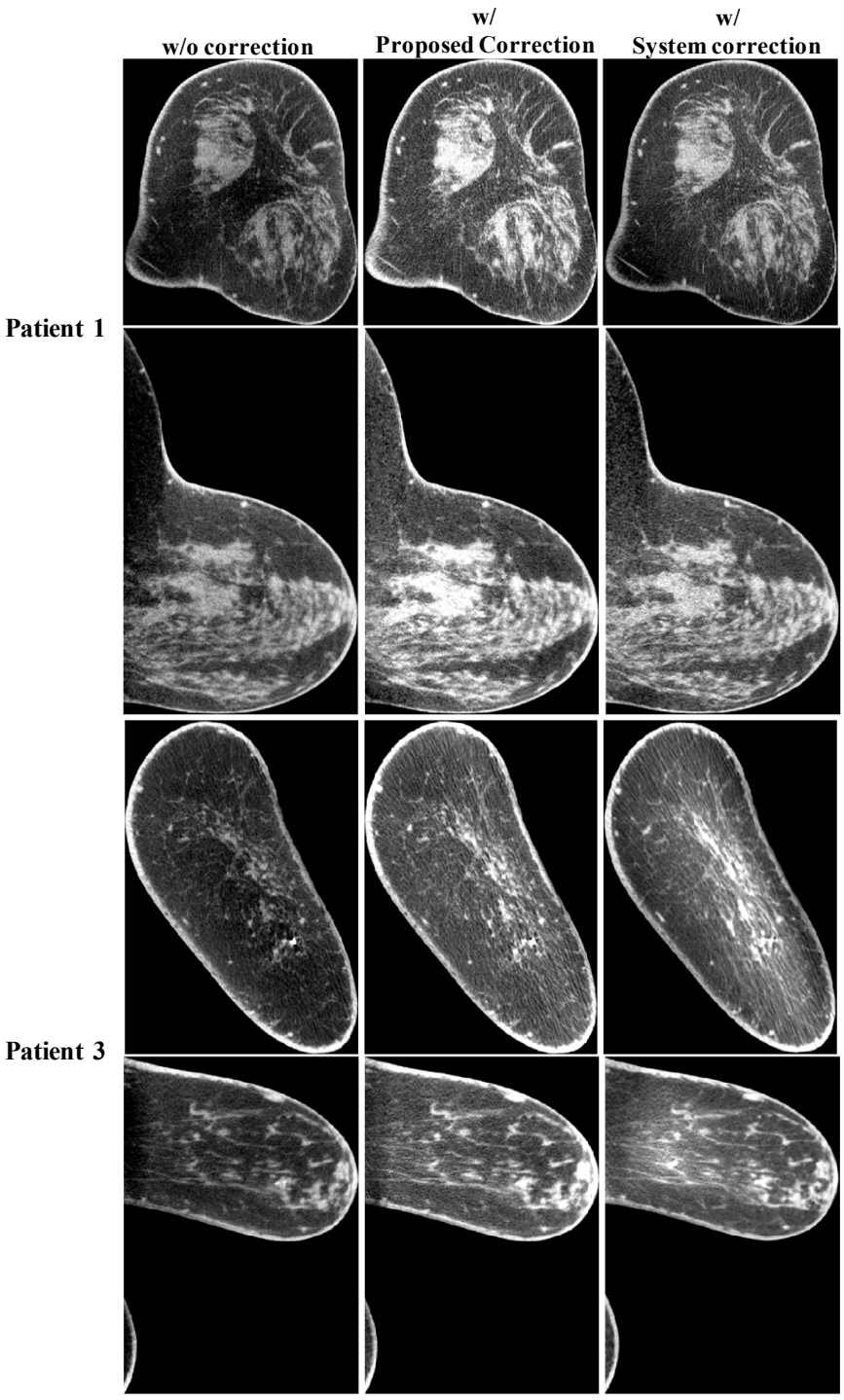

Fig 22 Comparison of the uncorrected image, the corrected image with the proposed scatter correction method and the corrected image with the system embedded software. The images are taken on Patient 1 and 3, but at slices different from those shown in Fig 19. Display window: [0.2 0.3] cm^{-1}.

Table 7 Comparison of SNU and CDR increase ratios using the proposed and the system scatter correction methods. Results are listed for both coronal and sagittal views.

Patient #	Coronal View					Sagittal View				
	SNU(%)			CDR Increase Ratio		SNU(%)			CDR Increase Ratio	
	w/o	Proposed	System	Proposed	System	w/o	Proposed	System	Proposed	System
1	8.31	2.25	7.64	1.52	1.13	12	4.52	9.75	1.87	1.2
3	2.12	1.91	7.33	1.26	0.66	5.46	2.35	3.86	1.16	1.03

3.4 Conclusions

In this work, we propose a highly practical and efficient scatter correction algorithm for CBBCT via a forward projection model. Scatter-free primary projections are first simulated by forward projecting the binary-object image segmented from the uncorrected CBBCT, and a first-pass scatter estimate is then generated by subtracting the simulated primary projection from the raw measured projection. Only sparse samples of the first-pass scatter estimate are used in the correction process to prevent tissue alteration caused by inaccurate segmentation. A Fourier-Transform based algorithm, local filtration, is applied to efficiently obtain a global scatter distribution. We evaluate the method performance on six patients with different breast sizes and shapes representing the general population. The results show that the proposed method effectively reduces the image SNU from 8.27% to 1.91% for coronal views and from 6.50% to 3.00% for sagittal views. The CDR is improved by an average factor of 1.41. Comparisons on the image details reveal that the proposed

scatter correction successfully preserves fine structures of fibroglandular tissues that are lost in the segmentation process.

Using subtraction-based signal processing, our method cannot remove scatter noise and therefore has limited improvement on CNR due to the increased CT image noise after scatter correction[87]. It is worth noting that, for practical implementations on clinical images, the term of CDR we use to quantify the image quality is different from CNR. In the CDR calculation, the image contrast is computed as the mean signal difference between adipose and glandular tissue. To obtain a background "noise" level, we first segment adipose tissue from the entire image and calculate the signal standard deviation as "noise". The calculated "noise" therefore includes statistical image noise as well as two additional terms: image non-uniformity due to image artifacts and small background structures. In our studies, we find that the standard deviation of adipose signals may decrease after scatter correction mainly due to the removal of the cupping artifacts, leading to a larger increase ratio on CDR than that on CNR.

The proposed method using a forward projection model is attractive in clinical CBBCT imaging for the following four features. First, the method is readily implementable on a clinical system as a software plug-in without modifications in current imaging protocols or system hardware. Second, the proposed algorithm does not make assumptions or approximations on the breast CT images, and therefore the method performance is expected to be more stable than those of other existing algorithms using simplified scatter models. Third, the proposed approach has a high computational efficiency as it uses linear filtering on sparse scatter samples (i.e., the local filtration technique). Lastly, since a mono-energetic x-ray spectrum is used in the forward projection, the simulated primary signals

do not contain beam-hardening errors and therefore the proposed algorithm potentially removes low-frequency beam-hardening errors as well.

The algorithm is currently implemented in MATLAB with hardware acceleration of one single GPU. To shorten the computation down to a clinical acceptable time, we will convert the MATLAB codes into more efficient languages (i.e. C, C++) and use parallel computing on a multi-GPU workstation. In addition, our future study will involve more patients to perform statistical analyses on the algorithm accuracy and stability. Human observer studies will be planned for investigations on the improvements in breast cancer detection enabled by the proposed method. A preliminary comparison between this forward-projection-based (FPB) method and the previously composed library-based (LB) method shows that the FPB method appears to better preserve the high spatial resolution details than the LB method. A detailed comparative study of the two approaches will be discussed in CHAPTER 4.

CHAPTER 4. INVESTIGATION THE EFFECT OF OFF-FOCUS RADIATION

4.1 Introduction

As discussed in the previous Chapters, we proposed two novel methods, using a library based technique [99] and a forward projection (FP) model [100]. In the LB method, a scatter library is precomputed based on a simplified semi-ellipsoidal breast model with different sizes. The scatter distribution is first selected from the library according to the breast size and then preprocessed and subtracted from the raw projection for scatter correction. In the FP method, scatter-free primary projection is first simulated by forward projecting the binary-object image segmented from the uncorrected CBBCT, and the final scatter distribution is obtained by subtraction of the simulated primary projection from the raw measured projection and local filtration [65], a specially designed technique which obtains a whole-field scatter distribution from sparse samples. Similar to the LB method, the acquired final scatter is finally subtracted from raw projections for effective scatter correction. Both LB and FP algorithms effectively remove scatter artifacts and improve image contrast on patient data.

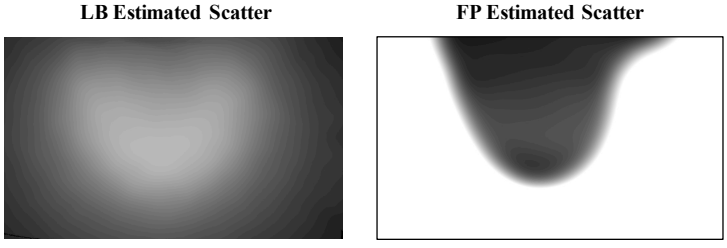

Fig 23 Example of the estimated scatter distributions by the LB (left) and the FP (right) methods. Display window: [100 2000] detector counts.

A somewhat surprising phenomenon we observe on the LB and FP methods is that, despite similar enhancement on CBBCT image qualities, these two methods obtain very different scatter distributions. One example is shown in Fig 23. It is worth noting that, in the existing literatures on scatter estimation/correction for CBCT imaging, scatter distributions similar to Fig 23(a) are commonly seen in MC-based methods [58, 61, 62], while measurement or analytical modeling based methods [53, 55] usually generate scatter distributions similar to Fig 23(b). In this work, we aim to identify the difference of physical modeling between the LB and FP methods that leads to different scatter estimates and to study its effect on the image quality of CBBCT. We find that the off-focus radiation (OFR) results in non-trivial signals in x-ray projections, which is ignored in the scatter estimation via the LB method. This finding is supported by experimental studies and its impact on the spatial resolution and contrast of CBBCT imaging is investigated using clinical data.

4.2 Methods and Materials

4.2.1 LB vs. FP scatter correction

We first briefly review the LB and FP algorithms for scatter correction in CBBCT, of which the major procedures are illustrated in Fig 24. The main differences between the two methods are bounded in the dashed squares.

In the LB method [99], a critical step is to obtain a scatter map from a scatter library based on the estimated breast diameter. The scatter library is pre-computed using MC simulations. In general, accurate scatter estimation in CBCT imaging requires a scatter library with a huge size (therefore tremendous computational burden) to accommodate different factors that contribute to changes of scatter, including scan geometry and object

distribution. The major contribution of our previous work [99] is that we develop a practical scatter correction method for CBBCT with a very small library and therefore achieve high efficacy and efficiency. Using clinical studies, we show that a scatter library with only one input parameter of the breast size is sufficient for effective scatter correction, due to the relative simplicity of breast geometry and composition.

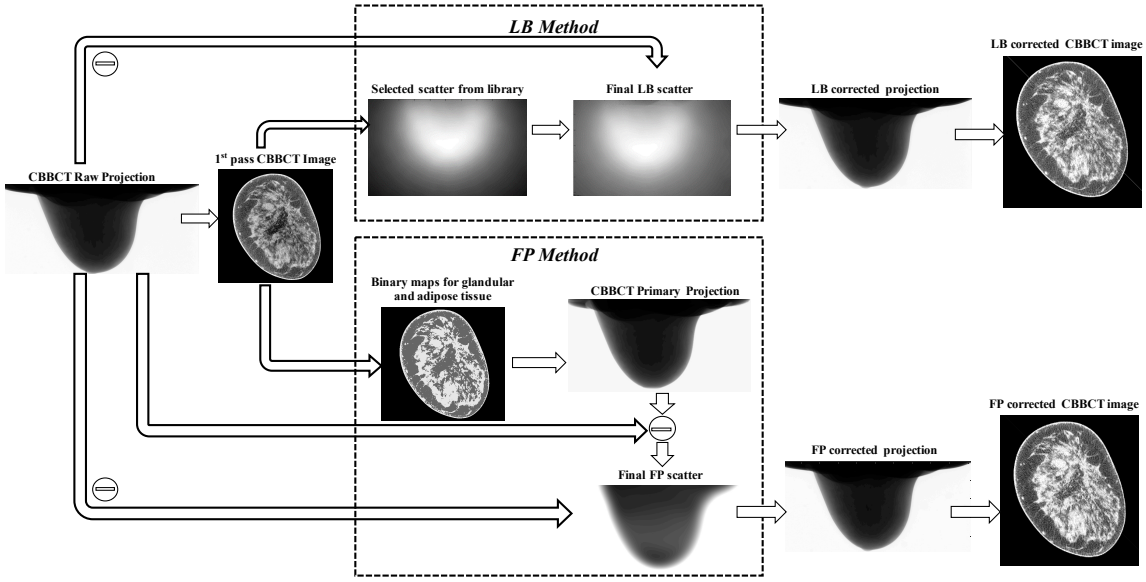

Fig 24 Workflows of the LB and FP methods. The dashed squares highlight the major differences.

A few approximations have to be in place in the LB method to simplify its implementation. An accurate distribution of the x-ray source is not only difficult to obtain but also shift variant on the detector [101]. As such, we use an ideal x-ray point source in the MC simulation for scatter library generation to save computation, and the scatter library therefore does not include OFR induced scatter signals. However, as we show in an earlier publication [101], in the current CBCT systems, OFR contributes 10% to 15% of the total radiation.

The FP method adopts a very different strategy of scatter estimation [100]. Instead of directly estimating the object scatter, a primary projection is simulated based on an ideal x-ray point source and then subtracted from the raw projection for a first scatter estimate. As a result, the obtained scatter distribution includes all signal components other than the primary signals, which consist of both the object scatter and the OFR induced scatter.

The difference between the LB and FP methods can be better explained using Eqn. (1) shown below. The measured raw projection in the unit of photon counts, I, contains three components, the primary signals, I_p, the object-induced scatter signals from the focal spot, I_s, and the additional scatter signals caused by OFR, I_{OFR}:

$$I = I_p + I_s + I_{OFR} \tag{14}$$

The FP method estimates scatter signals from $(I - I_p)$, and therefore I_{OFR} is removed after scatter correction, while the LB method estimates only I_s.

4.2.2 Effect of OFR on CBBCT

we aim to investigate the effect of I_{OFR} on the CBBCT image quality and then to compare the imaging performances of the LB and FP methods. OFR causes blurring on projection images. We first design experiments to measure the system point spread function (PSF) and modulation transfer function (MTF) on CBBCT with and without OFR. Clinical CBBCT images with scatter correction by the LB and FP methods are then evaluated and compared on the spatial resolution.

4.2.2.1 PSF and MTF measurements with and without OFR

All the measurements are carried out on the tabletop x-ray CBCT system in our lab [102]. The major components of our tabletop system match those of a clinical CBBCT system, which include a tungsten target x-ray tube (Varian RAD-94, Varian Medical Systems, Salt Lake City, UT), a Eureka MC150-C collimator, a thallium-doped Cesium Iodine (CsI:Tl) flat-panel detector (PaxScan® 4030CB, Varian Medical Systems, Salt Lake City, UT), and a rotary stage for CT data acquisition. To mimic the setup of the clinical research CBBCT prototype system used for the clinical data acquisition, the x-ray tube is operated at 50 kVp, 80 mA with a nominal focal spot size of 0.4 mm. The detector has an active area of 40 × 30 cm^2 running in a 2-by-2 binning mode with an effective detector pixel size of 0.388 × 0.388 mm^2. The frame rate of detector is set at 30 frames/s.

To avoid the object-induced scatter I_s and study the effect of only I_{OFR}, we scan a thin wire to generate a line-spread function (LSF) on the detector and then perform a standard filtered backprojection (FBP). The axial view of the reconstructed image is considered as the PSF of CBBCT. In the experiment, we place a copper-nickel wire with a diameter of 127 μm on the top of detector and perform an air scan without an object. In one of our previous studies, we show that x-ray beam collimation effectively reduces OFR on the detector [101]. We therefore repeat the experiment using a wide and a narrow collimator setting to obtain PSFs and MTFs with and without OFR. As shown in Fig 25, to remove most of I_{OFR}, only a small vertical region covering the thin wire is irradiated on the detector. In each measurement, 200 frames of projections are acquired and averaged to reduce the noise during data acquisition.

A one-dimensional LSF is first obtained from the projection on the thin wire. Each detector pixel value is considered as one sample of LSF at the location calculated as the

distance from the detector pixel to the wire center in the direction perpendicular to the wire. Note that, to ensure the data samples are more uniformly distributed, we intentionally place the wire in the vertical direction with a small oblique angle of about 1.4 degrees, as seen in Fig 25. The LSF is then generated via Gaussian fitting on these data samples, with a small sampling period of 0.025 mm, i.e., 1/15 of the detector pixel size.

To obtain the PSF of CBBCT, we assume that the calculated LSF results from the projection on a virtual wire located at the rotational center of the imaging system. Due to the rotational symmetry, the CBBCT image of the virtual wire, i.e. the PSF, is generated via FBP on 1000 identical LSFs, using geometric parameters of a clinical CBBCT system. The PSF image has a size of 1024 × 1024 pixels with an isotropic pixel size of 0.0125 mm. Note that, on our clinical prototype CBBCT, the source to axis of rotation distance is 650 mm and the source to the detector distance is 898 mm, resulting in a magnification factor of 1.38. The virtual wire therefore has a size of 92 μm (i.e., 127 μm/1.38).

The MTF computation from PSF is similar to the method proposed by Kwan et al [103]. A one-dimensional MTF is obtained via taking the magnitude of the Fourier Transform of the row-wise integration on the PSF image and then normalizing at the zero frequency.

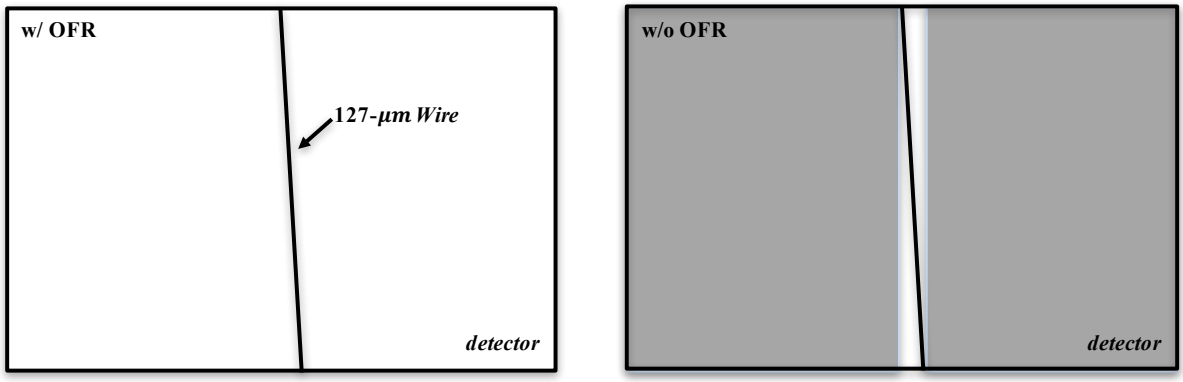

Fig 25 Experiment setups for PSF and MTF measurement with(left) and without(right) OFR.

4.2.2.2 Evaluation of clinical CBBCT images corrected using the LB and FP methods

The patient data presented in this work were acquired during a clinical research study under a protocol approved by the institutional review boards of the University of Rochester Medical Center and the University of Massachusetts Medical School. We first compare the image quality of the scatter corrected CBBCT images by the LB and FP methods. Small calcifications on the images are selected as point objects, on which PSFs are directly measured. MTFs are then calculated in the similar way as shown in the previous section.

The wire experiments of MTF measurements in the previous section show the improvement of image spatial resolution by removing OFR. To get rid of the effect of wire size on the MTF measurement, we quantify the improvement as the MTF ratio, which is computed as the ratio of spatial frequencies at different MTF values. As discussed earlier, we hypothesize that the LB and FP methods mainly differ in whether the OFR-induced signals are included after scatter correction. To verify this hypothesis, we compute the MTF ratios between the CBBCT images corrected by LB and FP and compare with those

obtained in the wire experiment. The two sets of MTF ratios are expected to match if the improvement of spatial resolution is indeed caused by the removal of OFR.

4.3 Results

4.3.1 Measured PSF and MTF with and without OFR

Fig 26 shows the Gaussian-fitted detector LSFs obtained from the wire experiment. It is seen that OFR degrades the spatial resolution with a larger full-width-at-half-maximum (FWHM) of LSF. The resultant CBBCT PSFs are shown in Fig 27. The central line profiles of the two PSFs (Fig 27 (c)) indicate that, in the absence of OFR, the FWHM of PSF decreases about 12% and the maximum signal of PSF increases about 14%.

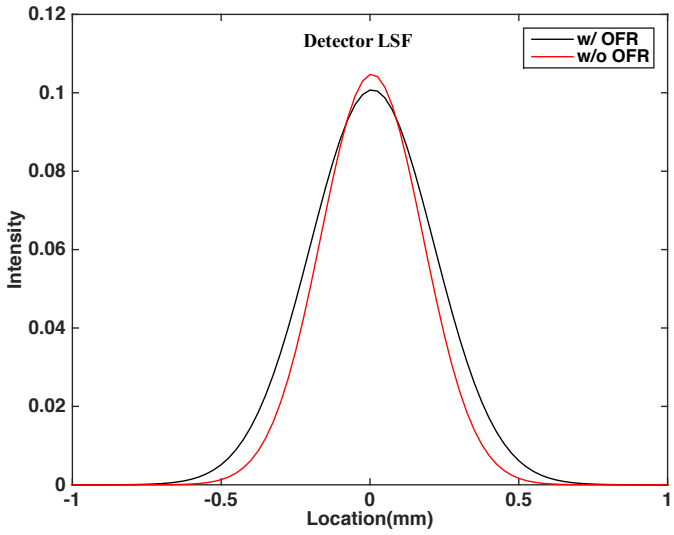

Fig 26 The Gaussian-fitted detector LSF w/ and w/o the OFR obtained from the wire experiment.

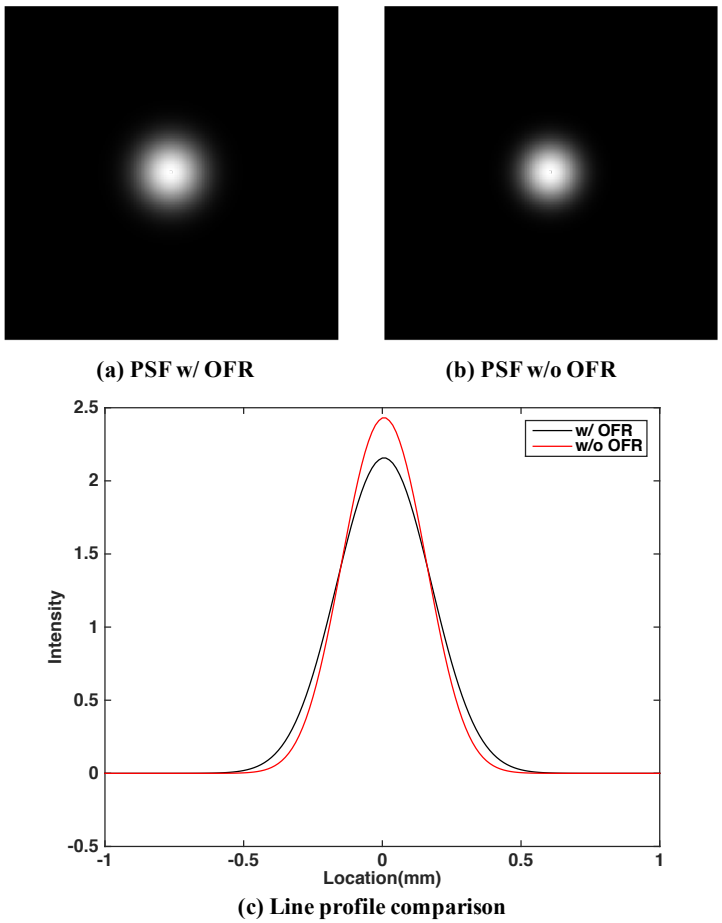

Fig 27 Zoom-in views (matrix size of 200×200 with a pixel size of 0.0125mm) of the reconstructed PSFs (a)with and (b)without OFR. (c) is the central line profile comparison for the two PSFs.

The effect of OFR on image spatial resolution is also seen in the MTF comparison shown in Fig 28. With OFR, the spatial frequencies at the MTF values of 50, 10, 5, and 0.5% are 1.13, 2.03, 2.30, and 3.01 lp/mm, respectively. Whereas without OFR, these spatial frequencies are 1.31, 2.34, 2.65, and 3.38 lp/mm, corresponding to an improvement of 16.1%, 15.5%, 15.1% and 12.1% at 50, 10, 5, and 0.5% MTF values, respectively.

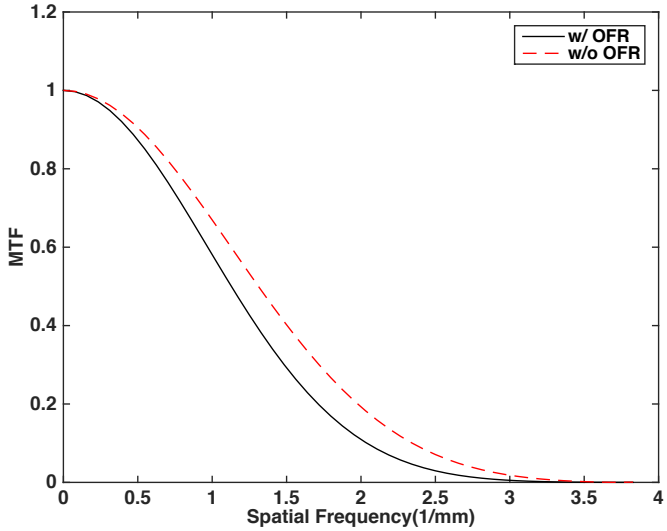

Fig 28 Comparison of the MTFs computed with and without OFR.

4.3.2 Evaluations of clinical CBBCT images

Fig 29 compares the scatter correction results using the LB and FP methods of four patients. It is observed that although both methods effectively remove the shading artifact caused by scatter and enhance the overall image contrast, the images corrected by FP appear to be crispier. This fact is better illustrated by plotting the one-dimensional profiles (see Fig 30) extracted from the dashed line passing through the calcifications. Compared with LB, the FP method increases the maximum signals of the line profiles by 14.5% and reduces the FWHMs by 12% on average. If we consider the line profiles passing through calcifications as analogs to image PSFs, the above result is consistent with what we found in the wire experiment.

We further compute "MTFs" from small regions of interest (ROIs) centered at calcifications as image "PSFs". In Fig 31, it is seen that the FP method achieves better

image spatial resolution than the LB method overall. Note that, these "MTFs" have different shapes because the calcifications have different physical sizes. We then calculate the improvement ratio of spatial frequencies at different MTF values and compare with that obtained from Fig 28 in the wire experiment. Fig 32 reveals that the improvement ratios are highly consistent with those of the wire experiment for all the patient cases, with an average root-mean-square difference of 0.47%.

The comparison of PSFs and MTFs show that the FP method outperforms the LB method on the image spatial resolution, and the improvement matches very well with the result of the wire experiment when OFR is suppressed. We therefore conclude that OFR causes the imaging difference between the FP and LB methods.

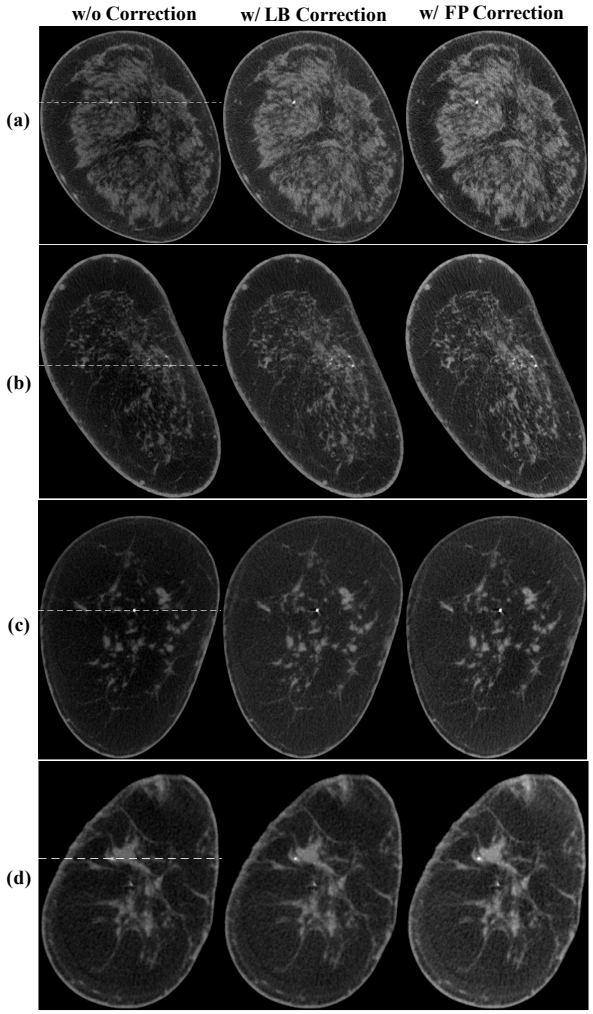

Fig 29 Comparison of CBBCT images in coronal views, obtained without scatter correction (first column), with the LB correction (second column) and with the FP correction (third column). Display window: [0.2 0.4] cm^{-1}.

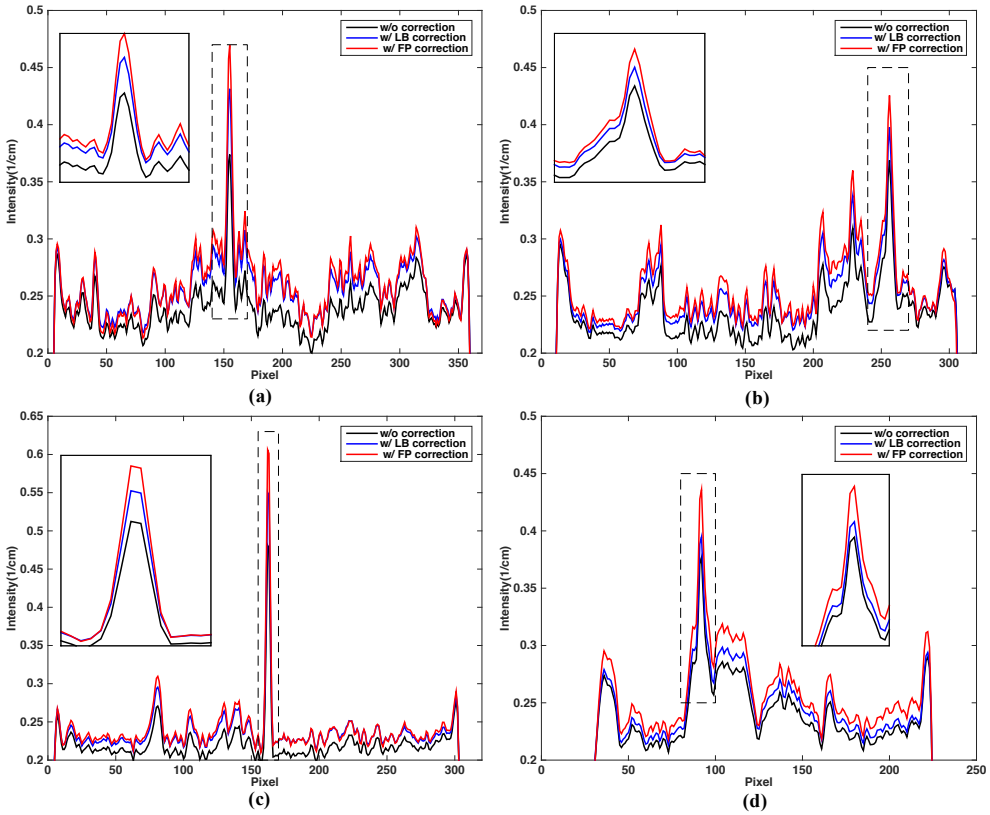

Fig 30 1-D profiles passing through the calcifications shown in Fig 29 (indicated as the dashed lines in the first column of Fig 29). The small window in each plot shows the zoom-in view of calcification peaks bounded in the dashed rectangle.

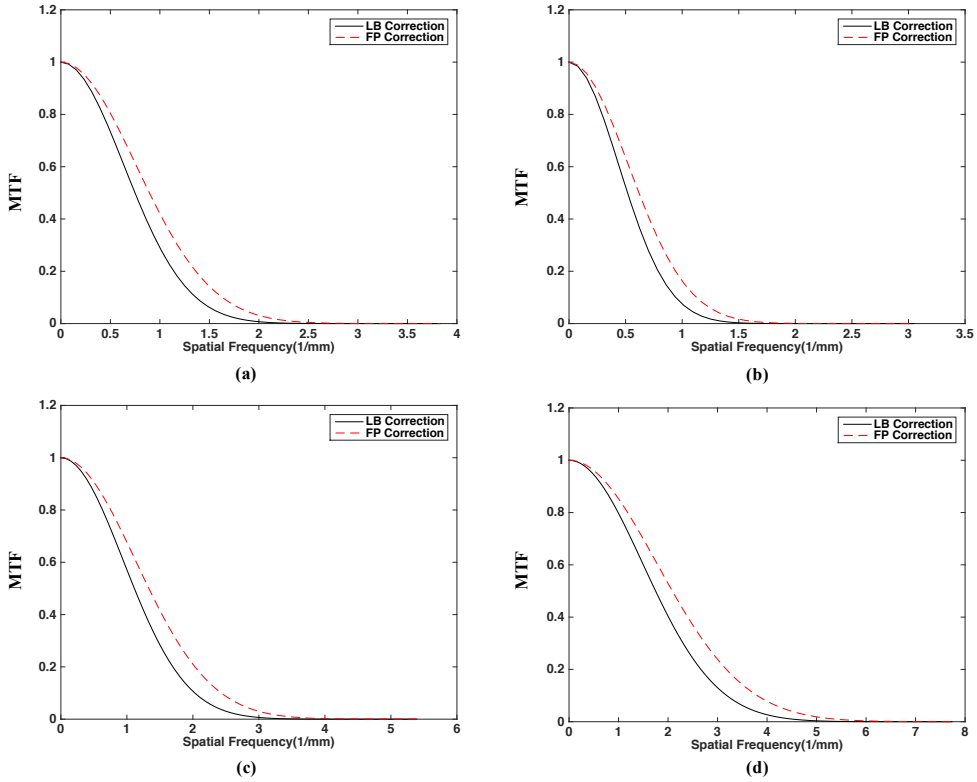

Fig 31 Comparison of the "MTFs" computed from the ROIs centered at calcification on the LB and FP corrected images.

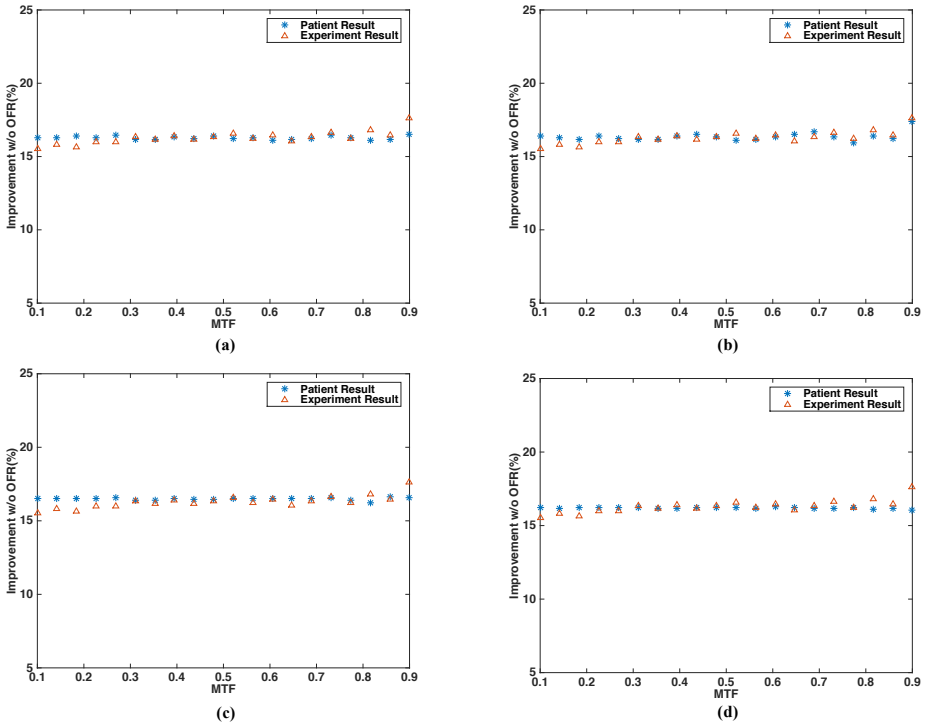

Fig 32 Comparison of the improvement ratios of spatial frequencies at different MTF values for each patient case shown in Fig 31 with the result of wire experiment shown in Fig 28.

4.4 Conclusions and Discussions

In this work, we compare the LB and FP methods and observe a significant difference in the scatter estimation. We hypothesize that the large discrepancy in the obtained scatter distributions is due to OFR, which is effectively removed only by the FP method, leading to improved image spatial resolution. To verify our hypothesis, a wire experiment is first designed to quantify the effect of OFR on the image spatial resolution. The results show that suppression of OFR increases the maximum signal of PSF by about 14% and reduces FWHM by about 12.0%. Similar improvement on spatial resolution is achieved by the FP method compared with the LB method in the study of four patients. The ratios of spatial frequencies at different MTF values with and without OFR match very well in both studies

at a level of around 16%, with an average root-mean-square difference of 0.47%. This result serves as a strong evidence that the FP method outperforms the LB method on image spatial resolution by removing OFR-induced signals.

Although the presented work is focused on comparisons of two recent scatter correction methods, our finding reveals an important fact that OFR, an error source considered as secondary in x-ray imaging, results in substantial difference of imaging performance in CBBCT. A critical requirement for a breast cancer diagnostic device is the ability to accurately detect micro-calcification as they are frequently the indications of malignancy [104, 105]. To date, many efforts have been exerted to optimize the detector performance of CBBCT system for better detection of micro-calcifications [106, 107], but there have not been any studies to investigate the dependency of OFR. The results presented in this study show that the OFR has a significant impact on the image quality in terms of spatial resolution and contrast, and this effect is especially prominent for fine structures (i.e., micro-calcifications) in CBBCT images. We believe that our finding is potentially important for enhancing the diagnostic performance of CBBCT in terms of calcification detection

CHAPTER 5. CONCLUSIONS AND FUTURE WORK

In this thesis, we proposed two scatter correction methods, library based and forward projection based, for quantitative dedicated CBBCT by exploring the uniqueness of this modality.

In library based method, we pre-compute a scatter library based on the simple shape and composition of the breast. A library size of 9 scatter images covering 6cm-22cm-diameter breast is sufficient to perform scatter correction with high efficacy and robustness for general women population.

In forward projection based method, making no assumption on the breast shape and composition, we first simulate the primary signals of projections via forward projection of the segmented first-pass CBBCT reconstruction. A raw scatter estimate containing both low-frequency scatter and errors is then obtained by subtracting the simulated primary projection from the raw projection. After discarding untrusted errors from the resultant raw scatter map, the final scatter is obtained via a novel Fourier-Transform based local filtration algorithm.

Both methods poise attractiveness in clinical adoption due to their high correction efficacy, high computational efficiency and easily implementation as a software plug-in without modifications in current imaging protocol or hardware.

By comparing these two proposed methods, we find that there is a large discrepancy between the scatter estimation of the two; and the FP based method tend to better preserve the high spatial resolution details than the LB method. We hypothesize that this is mainly

due to the existence of off-focus radiation (OFR), which is one fundamental factor degrading the image spatial resolution. To quantitatively investigate the effect of OFR on spatial resolution, we design an experiment to characterize the spatial resolution with and without OFR. We successfully validate our hypothesis by matching the experimental derivation to the results acquired from patient images corrected using the two correction methods. The results presented show that the OFR has a significant impact on the image quality in terms of spatial resolution and contrast. And this effect is especially prominent for fine structures (i.e., micro-calcifications) in CBBCT images.

Given the success of the quantitative dedicated CBBCT methods, we plan to carry out human observer studies on a large cohort of patients for investigations of the improvements in breast cancer detection. In addition, to enhance the clinical performance of CBBCT, our future study will also focus on developing generic approaches to remove OFR for improved spatial resolution of CBBCT.

REFERENCES

1. American Cancer Society. *Cancer Facts & Figures*. 2017 [cited 2017 30 March]; Available from: https://www.cancer.org/research/cancer-facts-statistics.html.

2. Siegel, R.L., K.D. Miller, and A. Jemal, *Cancer Statistics, 2017.* CA Cancer J Clin, 2017. **67**(1): p. 7-30.

3. Shapiro, S., P. Strax, and L. Venet, *Periodic breast cancer screening in reducing mortality from breast cancer.* JAMA, 1971. **215**(11): p. 1777-85.

4. Tabar, L., et al., *Efficacy of breast cancer screening by age. New results from the Swedish Two-County Trial.* Cancer, 1995. **75**(10): p. 2507-17.

5. Rosenberg, R.D., et al., *Effects of age, breast density, ethnicity, and estrogen replacement therapy on screening mammographic sensitivity and cancer stage at diagnosis: review of 183,134 screening mammograms in Albuquerque, New Mexico.* Radiology, 1998. **209**(2): p. 511-8.

6. Berry, D.A., et al., *Effect of screening and adjuvant therapy on mortality from breast cancer.* N Engl J Med, 2005. **353**(17): p. 1784-92.

7. Khalkhali, I., I. Mena, and L. Diggles, *Review of imaging techniques for the diagnosis of breast cancer: a new role of prone scintimammography using technetium-99m sestamibi.* Eur J Nucl Med, 1994. **21**(4): p. 357-62.

8. Karellas, A. and S. Vedantham, *Breast cancer imaging: a perspective for the next decade.* Med Phys, 2008. **35**(11): p. 4878-97.

9. Prasad, S.N. and D. Houserkova, *The role of various modalities in breast imaging.* Biomed Pap Med Fac Univ Palacky Olomouc Czech Repub, 2007. **151**(2): p. 209-18.

10. Kopans, D.B., *What is a useful adjunct to mammography?* Radiology, 1986. **161**(2): p. 560-1.

11. Kopans, D.B., *Proper utilization of mammography.* Am Fam Physician, 1986. **34**(1): p. 42.

12. Kopans, D.B., *Breast cancer detection.* West J Med, 1986. **144**(1): p. 73-6.

13. Hall, D.A., K.A. McCarthy, and D.B. Kopans, *Sonographic visualization of the normal postmenopausal ovary.* J Ultrasound Med, 1986. **5**(1): p. 9-11.

14. Berg, W.A., C.I. Campassi, and O.B. Ioffe, *Cystic lesions of the breast: sonographic-pathologic correlation.* Radiology, 2003. **227**(1): p. 183-91.

15. Kolb, T.M., J. Lichy, and J.H. Newhouse, *Comparison of the performance of screening mammography, physical examination, and breast US and evaluation of factors that influence them: an analysis of 27,825 patient evaluations.* Radiology, 2002. **225**(1): p. 165-75.

16. Tofts, P.S., B. Berkowitz, and M.D. Schnall, *Quantitative analysis of dynamic Gd-DTPA enhancement in breast tumors using a permeability model.* Magn Reson Med, 1995. **33**(4): p. 564-8.

17. Herborn, C.U., et al., *Breast augmentation and reconstructive surgery: MR imaging of implant rupture and malignancy.* Eur Radiol, 2002. **12**(9): p. 2198-206.

18. Muller-Schimpfle, M., et al., *Dynamic 3D-MR mammography: is there a benefit of sophisticated evaluation of enhancement curves for clinical routine?* J Magn Reson Imaging, 1997. **7**(1): p. 236-40.

19. Kristoffersen Wiberg, M., et al., *Value of MR imaging in clinical evaluation of breast lesions.* Acta Radiol, 2002. **43**(3): p. 275-81.

20. Liberman, L., et al., *MR imaging findings in the contralateral breast of women with recently diagnosed breast cancer.* AJR Am J Roentgenol, 2003. **180**(2): p. 333-41.

21. Park, J.M., et al., *Breast tomosynthesis: present considerations and future applications.* Radiographics, 2007. **27 Suppl 1**: p. S231-40.

22. Ciatto, S., et al., *Integration of 3D digital mammography with tomosynthesis for population breast-cancer screening (STORM): a prospective comparison study.* Lancet Oncol, 2013. **14**(7): p. 583-9.

23. Rafferty, E.A., et al., *Assessing radiologist performance using combined digital mammography and breast tomosynthesis compared with digital mammography alone: results of a multicenter, multireader trial.* Radiology, 2013. **266**(1): p. 104-13.

24. Zuley, M.L., et al., *Digital breast tomosynthesis versus supplemental diagnostic mammographic views for evaluation of noncalcified breast lesions.* Radiology, 2013. **266**(1): p. 89-95.

25. Michell, M.J., et al., *A comparison of the accuracy of film-screen mammography, full-field digital mammography, and digital breast tomosynthesis.* Clin Radiol, 2012. **67**(10): p. 976-81.

26. Skaane, P., et al., *Comparison of digital mammography alone and digital mammography plus tomosynthesis in a population-based screening program.* Radiology, 2013. **267**(1): p. 47-56.

27. Feng, S.S. and I. Sechopoulos, *Clinical digital breast tomosynthesis system: dosimetric characterization.* Radiology, 2012. **263**(1): p. 35-42.

28. O'Connor, M., D. Rhodes, and C. Hruska, *Molecular breast imaging.* Expert Rev Anticancer Ther, 2009. **9**(8): p. 1073-80.

29. Ersoy, R., et al., *Pituitary metastasis of breast cancer confirmed by fluorine-18 fluorodeoxyglucose positron emission tomography: a case report.* J Endocrinol Invest, 2007. **30**(6): p. 532-3.

30. Koga, S., et al., *[FDG-PET (positron emission tomography) in the detection of primary breast cancer and lymph node involvement].* Nihon Rinsho, 2007. **65 Suppl 6**: p. 379-84.

31. Vincentis, G.D., et al., *High resolution scintimammography helps in differentiating benign from malignant findings in scintigraphic hot spots.* Phys Med, 2006. **21 Suppl 1**: p. 87-90.

32. Scarfe, W.C. and A.G. Farman, *What is cone-beam CT and how does it work?* Dent Clin North Am, 2008. **52**(4): p. 707-30, v.

33. Robb, R.A., *The Dynamic Spatial Reconstructor: An X-Ray Video-Fluoroscopic CT Scanner for Dynamic Volume Imaging of Moving Organs.* IEEE Trans Med Imaging, 1982. **1**(1): p. 22-33.

34. Nemtoi, A., et al., *Cone beam CT: a current overview of devices.* Dentomaxillofac Radiol, 2013. **42**(8): p. 20120443.

35. Cho, P.S., R.H. Johnson, and T.W. Griffin, *Cone-beam CT for radiotherapy applications.* Phys Med Biol, 1995. **40**(11): p. 1863-83.

36. Martin, J., et al., *Building motion models of lung tumours from cone-beam CT for radiotherapy applications.* Phys Med Biol, 2013. **58**(6): p. 1809-22.

37. Chen, B. and R. Ning, *Cone-beam volume CT breast imaging: feasibility study.* Med Phys, 2002. **29**(5): p. 755-70.

38. Glick, S.J., *Breast CT.* Annu Rev Biomed Eng, 2007. **9**: p. 501-26.

39. Kwan, A.L., J.M. Boone, and N. Shah, *Evaluation of x-ray scatter properties in a dedicated cone-beam breast CT scanner.* Med Phys, 2005. **32**(9): p. 2967-75.

40. Kwan, A.L.C., J.M. Boone, and N. Shah, *Evaluation of x-ray scatter properties in a dedicated cone-beam breast CT scanner.* Medical Physics, 2005. **32**(9): p. 2967-2975.

41. Yang, X., et al., *Cupping artifact correction and automated classification for high-resolution dedicated breast CT images.* Med Phys, 2012. **39**(10): p. 6397-406.

42. Yang, K., G. Burkett, and J.M. Boone, *A breast-specific, negligible-dose scatter correction technique for dedicated cone-beam breast CT: a physics-based approach to improve Hounsfield Unit accuracy.* Phys Med Biol, 2014. **59**(21): p. 6487-505.

43. Zhu, L., et al., *Scatter correction for cone-beam CT in radiation therapy.* Med Phys, 2009. **36**(6): p. 2258-68.

44. Niu, T., et al., *Shading correction for on-board cone-beam CT in radiation therapy using planning MDCT images.* Med Phys, 2010. **37**(10): p. 5395-406.

45. Sechopoulos, I., *X-ray scatter correction method for dedicated breast computed tomography.* Med Phys, 2012. **39**(5): p. 2896-903.

46. Ramamurthy, S., C.J. D'Orsi, and I. Sechopoulos, *X-ray scatter correction method for dedicated breast computed tomography: improvements and initial patient testing.* Phys Med Biol, 2016. **61**(3): p. 1116-35.

47. Mail, N., et al., *The influence of bowtie filtration on cone-beam CT image quality.* Med Phys, 2009. **36**(1): p. 22-32.

48. Schafer, S., et al., *Antiscatter grids in mobile C-arm cone-beam CT: effect on image quality and dose.* Med Phys, 2012. **39**(1): p. 153-9.

49. Ruhrnschopf, E.P. and K. Klingenbeck, *A general framework and review of scatter correction methods in x-ray cone-beam computerized tomography. Part 1: Scatter compensation approaches.* Med Phys, 2011. **38**(7): p. 4296-311.

50. Sisniega, A., et al., *Monte Carlo study of the effects of system geometry and antiscatter grids on cone-beam CT scatter distributions.* Med Phys, 2013. **40**(5): p. 051915.

51. Siewerdsen, J.H., et al., *The influence of antiscatter grids on soft-tissue detectability in cone-beam computed tomography with flat-panel detectors.* Med Phys, 2004. **31**(12): p. 3506-20.

52. Endo, M., et al., *Effect of scattered radiation on image noise in cone beam CT.* Med Phys, 2001. **28**(4): p. 469-74.

53. Boone, J.M. and J.A. Seibert, *An analytical model of the scattered radiation distribution in diagnostic radiology.* Med Phys, 1988. **15**(5): p. 721-5.

54. Seibert, J.A. and J.M. Boone, *X-ray scatter removal by deconvolution.* Med Phys, 1988. **15**(4): p. 567-75.

55. Sun, M. and J.M. Star-Lack, *Improved scatter correction using adaptive scatter kernel superposition.* Phys Med Biol, 2010. **55**(22): p. 6695-720.

56. Li, H., R. Mohan, and X.R. Zhu, *Scatter kernel estimation with an edge-spread function method for cone-beam computed tomography imaging.* Phys Med Biol, 2008. **53**(23): p. 6729-48.

57. Kim, C., et al., *Data consistency-driven scatter kernel optimization for x-ray cone-beam CT.* Phys Med Biol, 2015. **60**(15): p. 5971-94.

58. Swindell, W. and P.M. Evans, *Scattered radiation in portal images: a Monte Carlo simulation and a simple physical model.* Med Phys, 1996. **23**(1): p. 63-73.

59. Bootsma, G.J., F. Verhaegen, and D.A. Jaffray, *Efficient scatter distribution estimation and correction in CBCT using concurrent Monte Carlo fitting.* Med Phys, 2015. **42**(1): p. 54-68.

60. Zbijewski, W. and F.J. Beekman, *Efficient Monte Carlo based scatter artifact reduction in cone-beam micro-CT.* IEEE Trans Med Imaging, 2006. **25**(7): p. 817-27.

61. Colijn, A.P. and F.J. Beekman, *Accelerated simulation of cone beam X-ray scatter projections.* IEEE Trans Med Imaging, 2004. **23**(5): p. 584-90.

62. Kyriakou, Y., T. Riedel, and W.A. Kalender, *Combining deterministic and Monte Carlo calculations for fast estimation of scatter intensities in CT.* Phys Med Biol, 2006. **51**(18): p. 4567-86.

63. Jarry, G., et al., *Characterization of scattered radiation in kV CBCT images using Monte Carlo simulations.* Med Phys, 2006. **33**(11): p. 4320-9.

64. Zhu, L., N.R. Bennett, and R. Fahrig, *Scatter correction method for X-ray CT using primary modulation: Theory and preliminary results.* Ieee Transactions on Medical Imaging, 2006. **25**(12): p. 1573-1587.

65. Zhu, L., *Local filtration based scatter correction for cone-beam CT using primary modulation.* Med Phys, 2016. **43**(11): p. 6199.

66. Siewerdsen, J.H., et al., *A simple, direct method for x-ray scatter estimation and correction in digital radiography and cone-beam CT.* Med Phys, 2006. **33**(1): p. 187-97.

67. Cai, W., R. Ning, and D. Conover, *Scatter correction for clinical cone beam CT breast imaging based on breast phantom studies.* J Xray Sci Technol, 2011. **19**(1): p. 91-109.

68. Niu, T.Y. and L. Zhu, *Overview of X-ray Scatter in Cone-beam Computed Tomography and Its Correction Methods.* Current Medical Imaging Reviews, 2010. **6**(2): p. 82-89.

69. Ruhrnschopf, Ep, and K. Klingenbeck, *A general framework and review of scatter correction methods in cone beam CT. Part 2: scatter estimation approaches.* Med Phys, 2011. **38**(9): p. 5186-99.

70. Ning, R., X. Tang, and D. Conover, *X-ray scatter correction algorithm for cone beam CT imaging.* Med Phys, 2004. **31**(5): p. 1195-202.

71. Altunbas, M.C., et al., *A post-reconstruction method to correct cupping artifacts in cone beam breast computed tomography.* Med Phys, 2007. **34**(7): p. 3109-18.

72. O'Connell, A., et al., *Cone-beam CT for breast imaging: Radiation dose, breast coverage, and image quality.* AJR Am J Roentgenol, 2010. **195**(2): p. 496-509.

73. Boone, J.M., et al., *Dedicated breast CT: radiation dose and image quality evaluation.* Radiology, 2001. **221**(3): p. 657-67.

74. Sechopoulos, I., et al., *Monte Carlo and phantom study of the radiation dose to the body from dedicated CT of the breast.* Radiology, 2008. **247**(1): p. 98-105.

75. Vedantham, S., et al., *Personalized estimates of radiation dose from dedicated breast CT in a diagnostic population and comparison with diagnostic mammography.* Phys Med Biol, 2013. **58**(22): p. 7921-36.

76. Thacker, S.C. and S.J. Glick, *Normalized glandular dose (DgN) coefficients for flat-panel CT breast imaging.* Phys Med Biol, 2004. **49**(24): p. 5433-44.

77. Boone, J.M., N. Shah, and T.R. Nelson, *A comprehensive analysis of DgN(CT) coefficients for pendant-geometry cone-beam breast computed tomography.* Med Phys, 2004. **31**(2): p. 226-35.

78. Yaffe, M.J., et al., *The myth of the 50-50 breast.* Medical Physics, 2009. **36**(12): p. 5437-5443.

79. Vedantham, S., et al., *Dedicated breast CT: fibroglandular volume measurements in a diagnostic population.* Med Phys, 2012. **39**(12): p. 7317-28.

80. Wiegert, J., et al., *Model based scatter correction for cone-beam computed tomography.* Medical Imaging 2005: Physics of Medical Imaging, Pts 1 and 2, 2005. **5745**: p. 271-282.

81. Spies, L., et al., *Direct measurement and analytical modeling of scatter in portal imaging.* Medical Physics, 2000. **27**(3): p. 462-471.

82. D'Errico, J. *Surface Fitting using gridfit*. 2010; Available from: http://www.mathworks.com/matlabcentral/fileexchange/8998-surface-fitting-using-gridfit.

83. Huang, S.Y., et al., *The characterization of breast anatomical metrics using dedicated breast CT.* Med Phys, 2011. **38**(4): p. 2180-91.

84. D'Orsi, C.J., et al., *2013 ACR BI-RADS Atlas: Breast Imaging Reporting and Data System*. 2013: Reston, VA, American College of Radiology.

85. Vedantham, S., et al., *Dedicated breast CT: radiation dose for circle-plus-line trajectory.* Med Phys, 2012. **39**(3): p. 1530-41.

86. Sechopoulos, I., S.S. Feng, and C.J. D'Orsi, *Dosimetric characterization of a dedicated breast computed tomography clinical prototype.* Med Phys, 2010. **37**(8): p. 4110-20.

87. Zhu, L., J. Wang, and L. Xing, *Noise suppression in scatter correction for cone-beam CT.* Med Phys, 2009. **36**(3): p. 741-52.

88. Shi, L., et al., *Library-based scatter correction for dedicated cone beam breast CT: a feasibility study*, in *Proc. SPIE*. 2016.

89. Vedantham, S., L. Shi, and A. Karellas, *TU-CD-207-10: Dedicated Cone-Beam Breast CT: Design of a 3-D Beam-Shaping Filter.* Medical Physics, 2015. **42**(6): p. 3612-3612.

90. O'Connell, A.M., A. Karellas, and S. Vedantham, *The potential role of dedicated 3D breast CT as a diagnostic tool: review and early clinical examples.* Breast J, 2014. **20**(6): p. 592-605.

91. Sanchez, A.A., E.Y. Sidky, and X. Pan, *Task-based optimization of dedicated breast CT via Hotelling observer metrics.* Med Phys, 2014. **41**(10): p. 101917.

92. Jalalian, A., et al., *Computer-aided detection/diagnosis of breast cancer in mammography and ultrasound: a review.* Clin Imaging, 2013. **37**(3): p. 420-6.

93. Malich, A., et al., *Effect of breast density on computer aided detection.* J Digit Imaging, 2005. **18**(3): p. 227-33.

94. Rangayyan, R.M., F.J. Ayres, and J.E. Leo Desautels, *A review of computer-aided diagnosis of breast cancer: Toward the detection of subtle signs.* Journal of the Franklin Institute, 2007. **344**(3–4): p. 312-348.

95. Castellino, R.A., *Computer aided detection (CAD): an overview.* Cancer Imaging, 2005. **5**: p. 17-9.

96. Fraioli, F., G. Serra, and R. Passariello, *CAD (computed-aided detection) and CADx (computer aided diagnosis) systems in identifying and characterising lung nodules on chest CT: overview of research, developments and new prospects.* Radiol Med, 2010. **115**(3): p. 385-402.

97. Niu, T.Y., A. Al-Basheer, and L. Zhu, *Quantitative cone-beam CT imaging in radiation therapy using planning CT as a prior: First patient studies.* Medical Physics, 2012. **39**(4): p. 1991-2000.

98. Siddon, R.L., *Fast calculation of the exact radiological path for a three-dimensional CT array.* Med Phys, 1985. **12**(2): p. 252-5.

99. Shi, L., et al., *Library based x-ray scatter correction for dedicated cone beam breast CT.* Med Phys, 2016. **43**(8): p. 4529.

100. Shi, L., et al., *X-ray scatter correction for dedicated cone beam breast CT using a forward projection model.* Med Phys, 2017.

101. Dong, X., et al., *Relationship between x-ray illumination field size and flat field intensity and its impacts on x-ray imaging.* Med Phys, 2012. **39**(10): p. 5901-9.

102. Niu, T. and L. Zhu, *Scatter correction for full-fan volumetric CT using a stationary beam blocker in a single full scan.* Med Phys, 2011. **38**(11): p. 6027-38.

103. Kwan, A.L., et al., *Evaluation of the spatial resolution characteristics of a cone-beam breast CT scanner.* Med Phys, 2007. **34**(1): p. 275-81.

104. Frankl, G. and M. Ackerman, *Xeromammography and 1200 breast cancers.* Radiol Clin North Am, 1983. **21**(1): p. 81-91.

105. Moskowitz, M., *The predictive value of certain mammographic signs in screening for breast cancer.* Cancer, 1983. **51**(6): p. 1007-11.

106. Shen, Y., et al., *Cone beam breast CT with a high pitch (75 mum), thick (500 mum) scintillator CMOS flat panel detector: visibility of simulated microcalcifications.* Med Phys, 2013. **40**(10): p. 101915.

107. Gazi, P.M., et al., *Evolution of spatial resolution in breast CT at UC Davis.* Med Phys, 2015. **42**(4): p. 1973-81.